

AD-A032 311

ATMOSPHERIC SCIENCE ASSOCIATES BEDFORD MASS
ADDITIONAL STUDIES OF THE EFFECTS OF AIRPLANE FLOWFIELDS ON HYD--ETC(U)
AUG 76 H G NORMENT

F/G 4/2

F19628-76-C-0142

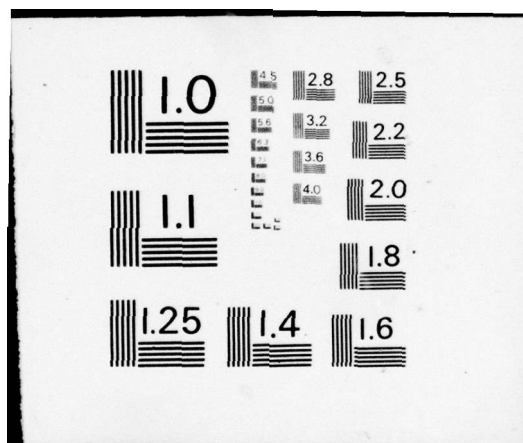
UNCLASSIFIED

AFGL-TR-76-0187

NL

1 of 1
ADA032311





AD A032311

AFGL-TR-76-0187

ADDITIONAL STUDIES OF THE EFFECTS OF AIRPLANE
FLOWFIELDS ON HYDROMETEOR CONCENTRATION
MEASUREMENTS

Hillyer G. Norment

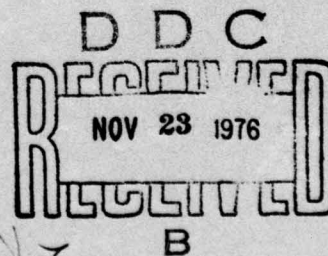
Atmospheric Science Associates
363 Great Road
P.O. Box 307
Bedford, Massachusetts 01730

13 August 1976

Final Report for Period 7 January 1976 - 13 August 1976

Approved for public release; distribution unlimited

AIR FORCE GEOPHYSICS LABORATORY
AIR FORCE SYSTEMS COMMAND
UNITED STATES AIR FORCE
HANSOM AFB, MASSACHUSETTS 01731



S/C
392152

Qualified requestors may obtain additional copies from the Defense Documentation Center. All others should apply to the National Technical Information Service.

Unclassified

SECURITY CLASSIFICATION OF THIS PAGE (When Data Entered)

REPORT DOCUMENTATION PAGE		READ INSTRUCTIONS BEFORE COMPLETING FORM
1. REPORT NUMBER <u>18</u> AFGL-TR-76-0187	2. GOVT ACCESSION NO. <u>9</u> Final rept. 7 Jan - 13 Aug 76	3. RECIPIENT'S CATALOG NUMBER
4. TITLE (and Subtitle) ADDITIONAL STUDIES OF THE EFFECTS OF AIRPLANE FLOWFIELDS ON HYDROMETEOR CONCENTRATION MEASUREMENTS		5. TYPE OF REPORT & PERIOD COVERED Scientific - Final 1/7/76 - 7/13/76
7. AUTHOR(s) <u>10</u> Hillyer G. Norment		6. PERFORMING ORG. REPORT NUMBER
9. PERFORMING ORGANIZATION NAME AND ADDRESS Atmospheric Science Associates P.O. Box 307 Bedford, Massachusetts		8. CONTRACT OR GRANT NUMBER(s) <u>15</u> F19628-76-C-0142
11. CONTROLLING OFFICE NAME AND ADDRESS Air Force Geophysics Laboratory (LYC) Hanscom AFB, Massachusetts 01731 Contract Monitor: Mr. Morton Glass		10. PROGRAM ELEMENT, PROJECT, TASK AREA & WORK UNIT NUMBERS 63311F <u>16</u> 627A0001 <u>17</u> 00
14. MONITORING AGENCY NAME & ADDRESS (if different from Controlling Office)		12. REPORT DATE <u>11</u> 13 August 1976
		13. NUMBER OF PAGES 66 <u>12</u> 600
		15. SECURITY CLASS. (of this report) Unclassified
		15a. DECLASSIFICATION/DOWNGRADING SCHEDULE
16. DISTRIBUTION STATEMENT (of this Report) Approved for public release; distribution unlimited		
17. DISTRIBUTION STATEMENT (of the abstract entered in Block 20, if different from Report)		
18. SUPPLEMENTARY NOTES		
19. KEY WORDS (Continue on reverse side if necessary and identify by block number) cloud physics large particle trajectory calculations water drop concentration meteorological research airplanes ice crystal concentration effect of airflow on particle concentration concentration factor calibration of airborne hydrometeor samplers Learjet 36		
20. ABSTRACT (Continue on reverse side if necessary and identify by block number) Hydrometeor concentrations seen by fuselage-mounted particle sampling instruments are distorted owing to flow around the airplane. A general, three-dimensional method is used to compute concentration distortion and sampling efficiency. Evidence to support the use of steady-state drag coefficients for accelerative particle motion is discussed. Assessments of sampling adequacies of several instruments mounted on a Learjet 36 airplane are reported. This includes a total water content indicator mounted		

next
page

DD FORM 1 JAN 73 1473

EDITION OF 1 NOV 65 IS OBSOLETE

Unclassified

SECURITY CLASSIFICATION OF THIS PAGE (When Data Entered)

392 152
600

Unclassified

SECURITY CLASSIFICATION OF THIS PAGE(When Data Entered)

20.

cont

→ inside the nose of the Learjet, assessment of which requires calculation of air and particle flow into the instrument orifice - a new application of the method. Finally, a preliminary, generalized method is developed for estimation of "safe" sampling distances for fuselage-mounted instruments and results are compared with those of case studies. ↑

ACCESSION FOR	
REFS	WHICH SECTION <input checked="" type="checkbox"/>
C. S.	DIFF. SECTION <input type="checkbox"/>
ORAL. BRIDGE	<input type="checkbox"/>
ADDITIONAL	
BY	
DISTRIBUTION/AVAILABILITY	
Q101	AVAIL. OR. OF C. S.
A	

Unclassified

SECURITY CLASSIFICATION OF THIS PAGE(When Data Entered)

PREFACE

The author acknowledges with gratitude the support and guidance of Morton Glass and Robert Cunningham of the Meteorology Division, AFGL.

The project was supported by AFGL as part of the Advanced Ballistics Reentry Systems (ABRES) program.

TABLE OF CONTENTS

	<u>Page</u>
INTRODUCTION	1
BACKGROUND	2
NATURE OF THE PROBLEM	2
CONCENTRATION FACTOR	2
PARTICLE TRAJECTORY CALCULATION	4
THREE-DIMENSIONAL FLOW CALCULATION	7
PARTICLE DRAG COEFFICIENT	9
LEARJET 36	11
INSTRUMENT LOCATIONS	11
RESULTS FOR THE SNOW STICK, REPLICATOR AND ASP	14
PARTICLE TRAJECTORY ANGLE AT THE 1-D PARTICLE SPECTROMETERS	21
TOTAL WATER CONTENT INDICATOR	21
<u>Instrument Description</u>	21
<u>Flowfield Studies</u>	23
<u>Concentration Factors, Concentration Ratios and</u>	
<u>Concentration Correction Factors</u>	23
GENERALIZATION OF THE CONCENTRATION FACTOR METHOD FOR FUSELAGE-MOUNTED INSTRUMENTS	40
INTRODUCTION	40
CONCENTRATION FACTOR RESULTS FOR POTENTIAL FLOW AROUND AN ISOLATED POINT SOURCE	40
COMPARISON WITH CASE STUDY RESULTS	48
SUMMARY AND CONCLUSIONS	52
APPENDIX	54
REFERENCES	56

LIST OF FIGURES

<u>Figure Number</u>		<u>Page</u>
1	Trajectories of 100 μm diameter water drops in potential airflow about a prolate ellipsoid of fineness ratio 2. (The ordinate scale is expanded by a factor of 2.)	3
2	Perspective view of a particle flux tube.	5
3	Computer prepared plots of the digital description of the Learjet 36 fuselage.	8
4	Learjet 36.	12
5	Learjet 36 with instruments mounted.	13
6	Computer prepared plot showing a segment of trajectory for a 300 μm diameter water drop to one of the PMS 1-D particle spectrometers. The airplane axis is inclined at 4.5 degrees to the horizontal.	22
7	Special digital description of the Learjet 36 nose for the TWCI study.	24
8a	Flowfield around the Learjet 36 nose tip in the plane $y=0$ for zero intake into the TWCI orifice.	25
8b	Flowfield around the Learjet 3 nose tip in the plane $y=0$ for intake of 5% of the freestream flow into the TWCI orifice.	26
8c	Flowfield around the Learjet 36 nose tip in the plane $y=0$ for intake of 100% of the freestream flow into the TWCI orifice.	27
9	Stereo view of 100 μm diameter water drop trajectories to the Learjet 36 nose. Intake of the TWCI orifice is 5% of the freestream flow.	28
10	Stereo view of a flux tube of 10 μm diameter water drops to the Learjet 36 TWCI orifice.	31
11	Target and initial plane flux tube cross sections for 10 μm diameter water drops to the TWCI orifice.	32
12	Reciprocal concentration factor vs. particle mass for various hydrometeors as collected by the Learjet 36 TWCI.	38

LIST OF FIGURES (continued)

<u>Figure Number</u>		<u>Page</u>
13	Trajectories of 10 μm diameter water drops in potential airflow around a single point source which simulates a fuselage of radius 0.8 m with velocity 130 m sec^{-1} at 20 kft altitude. These trajectories virtually coincide with airflow streamlines.	41
14a	Trajectories of 100 μm diameter water drops through a potential flow field around a single point source. These calculations simulate a fuselage of radius 0.8 m with velocity 130 m sec^{-1} at 20 kft altitude.	42
14b	Trajectories of 100 μm diameter water drops through a potential flow field around a single point source. These calculations simulate a fuselage of radius 2.0 m with velocity 130 m sec^{-1} at 20 kft altitude.	43
15	Trajectories of 1000 μm diameter water drops in potential airflow around a single point source. These calculations simulate a fuselage of radius 0.8 m with velocity 130 m sec^{-1} at 20 kft altitude. The tilt of the trajectories is caused by gravity settling.	44
16	Cross section of simulated fuselage showing concentration factor calculation geometry used for the generalization calculations.	46
17	Summary of concentration factor results that bracket the shadow zone edge.	47
18	Fuselage radius, y_s vs. distance aft from the nose tip, x , for various airplane fuselages and the point source body.	50

LIST OF TABLES

<u>Table Number</u>		<u>Page</u>
1	COORDINATES OF INSTRUMENT SAMPLING POINTS ON THE LEARJET 36	15
2	WATER DROP CONCENTRATION FACTORS AT THE LEARJET 36 SNOW STICK, FORMVAR REPLICATOR and ASP	16
3	SHADOW ZONE BRACKETING FOR INSTRUMENTS ON THE LEARJET 36	17
4	PROPERTIES OF COLUMNAR ICE CRYSTALS	18
5	PROPERTIES OF HEXAGONAL PLATE (Pl _a) ICE CRYSTALS	19
6	ICE CONCENTRATION FACTORS AT THE LEARJET 36 SNOW STICK	20
7	WATER DROP CONCENTRATION RATIOS AT THE LEARJET 36 TWCI FOR 5% AIR INTAKE	30
8	PROPERTIES OF PLANE DENDRITIC (Pl _e) ICE CRYSTALS	34
9	PROPERTIES OF AGGREGATES OF UNRIMED RADIATING ASSEMBLAGES OF PLATES, SIDE PLANES, BULLETS AND COLUMNS	34
10	ICE COLUMN CONCENTRATION RATIOS AT THE LEARJET 36 TWCI	35

LIST OF TABLES (continued)

<u>Table Number</u>		<u>Page</u>
11	HEXAGONAL PLATE (P1a) CONCENTRATION RATIOS AT THE LEARJET 36 TWCI	36
12	PLANE DENDRITE (P1e) CONCENTRATION RATIOS AT THE LEARJET 36 TWCI	37
13	CRYSTAL AGGREGATE CONCENTRATION RATIOS AT THE LEARJET 36 TWCI	37
14	SUMMARY OF CASE-STUDY CONCENTRATION FACTOR RESULTS	49

INTRODUCTION

Hydrometeor concentrations aloft are determined by radar and by airplane-mounted samplers. Radar measurements are strongly biased toward larger particle sizes, and do not discriminate between hydrometeor types. Airplane samples can be used to calibrate the radar measurements, identify hydrometeor types, and fill out the small-particle tails of the size distributions.

One of the problems with airplane sampling of hydrometeors is that hydrometeor concentrations tend to be distorted at sampling points near the fuselage surface. This report is concerned with theoretical assessment of this distortion for specific airplane-mounted instruments. Theoretical bases of the method used and several applications are presented in refs. 1 and 2. A summary of the theory is given in the next section.

In this report, additional support for use of steady-state drag coefficients for calculation of accelerative particle motion is discussed. Assessments of sampling adequacies of several instruments mounted on a Learjet 36 airplane are reported. This includes assessment of a total water content indicator in the nose of the Learjet that requires computation of flow into the airplane nose: a new application of the method. Finally, results of a preliminary attempt to prepare a generalized graph to be used to estimate "safe" sampling distances for fuselage-mounted instruments are compared with results obtained from a number of specific studies.

1. H.G. Norment and R.G. Zalosh, "Effects of Airplane Flowfields on Hydrometeor Concentration Measurements", AFCRL-TR-74-0602 (6 Dec. 1974). AD-A006 690.
2. H.G. Norment, "Effects of Airplane Flowfields on Cloud Water Content Measurements", AFCRL-TR-75-0231 (30 April 1975). AD-A014 807.

BACKGROUND

NATURE OF THE PROBLEM

Particle sampling devices of interest here usually measure particle flux through a small space adjacent to an airplane fuselage. Unless the sampling space is distant enough from the airplane to be in the free-stream, particles of certain sizes will interact with the flow about the fuselage to cause flux distortion. The situation is illustrated in Fig. 1 for 100 μ m diameter water drops in airflow about a prolate ellipsoid of fineness ratio 2. Note the impaction on the ellipsoid of the drop closest to the ellipsoid symmetry axis, and note the substantial deflections of the next closest trajectories. Trajectory deflection causes high particle concentrations and high concentration gradients to be observed at a point such as the one marked (X)1 in the figure. At point (X)2, deflection and impaction combine to produce a region void of particles, a so-called "shadow zone". Smaller drops, with much less inertia, tend to follow the airflow more exactly such that less distortion is observed. Drops large enough to have very high inertia substantially ignore the airflow, and again little distortion is observed. Therefore, distortion is significant over a limited range of particle sizes.

CONCENTRATION FACTOR

Principal results of this work are expressed in a quantity called concentration factor. Concentration factor, C_F , is defined as the ratio of particle flux at the sampling or target point, F_t , to the particle flux in the freestream, F ,

$$C_F \equiv \frac{F_t}{F} . \quad (1)$$

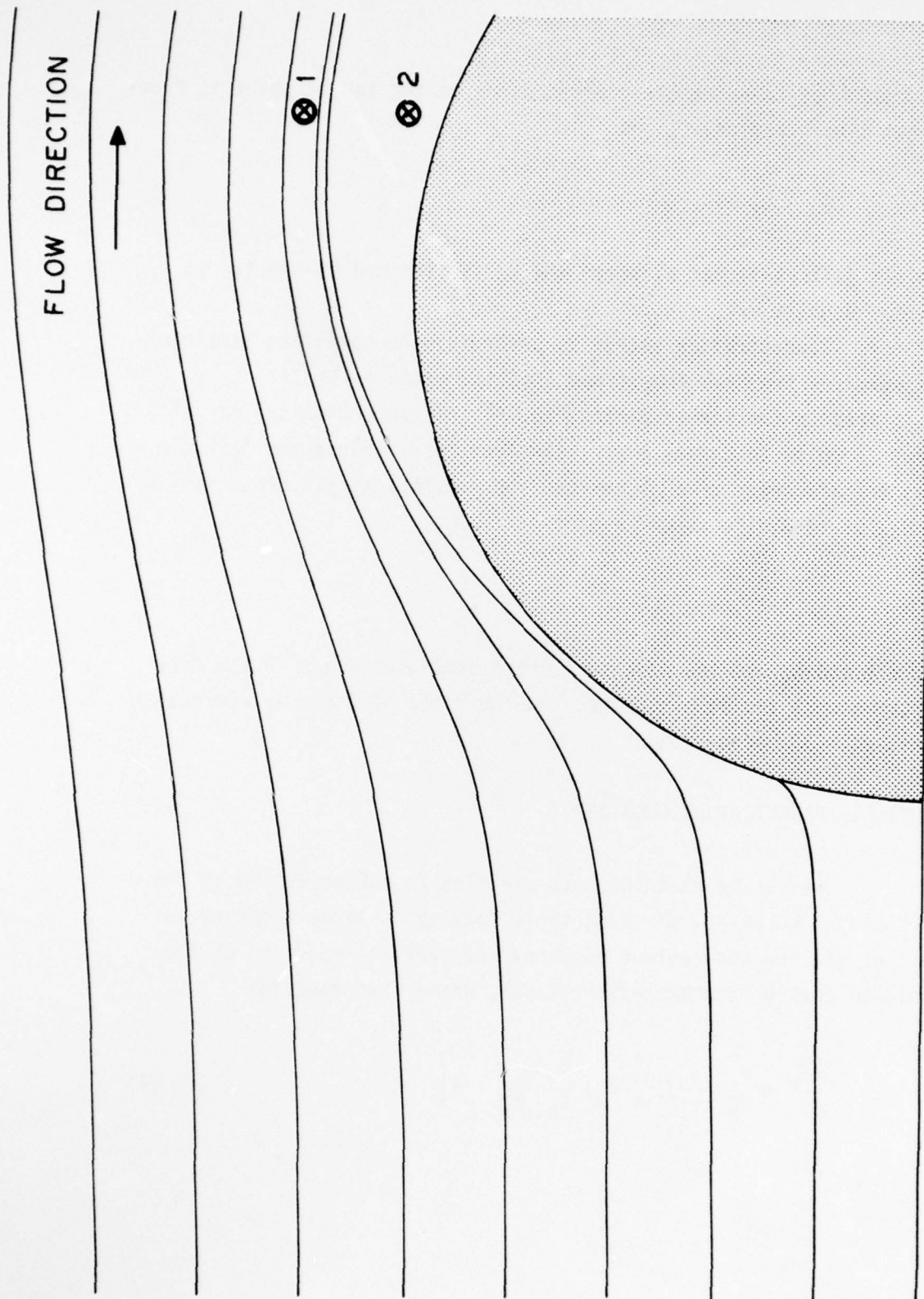


Figure 1. Trajectories of $100\text{ }\mu\text{m}$ diameter water drops in potential airflow about a prolate ellipsoid of fineness ratio 2. (The ordinate scale is expanded by a factor of 2.)

The ratio of the particle concentration at the target point to free-stream concentration, C_M , is

$$C_M \approx C_F V/V_t, \quad (2)$$

where V is free-stream airspeed and V_t is airspeed at the target point. Usually $V/V_t \approx 1$.

Concentration factor is determined by computing particle trajectories from the freestream (initial plane in Fig. 2) to a small area in the target plane (Fig. 2) that surrounds the target point such as to define a particle flux tube. Since the particle mass transfer rate through the tube is constant at all cross sections, it is easily shown that

$$C_F \approx \frac{A}{A_t}, \quad (3)$$

where A and A_t are the flux tube cross sectional areas in the free-stream and at the target point. In the limit as A and A_t approach zero, eq. (3) becomes exact.

PARTICLE TRAJECTORY CALCULATION

We assume that the bulk air flow is not perturbed by the particles. Moreover, since particle density is large compared to that of air, we can neglect buoyancy and inertial reaction of the fluid to obtain the three-dimensional, normalized equation

$$\frac{d\vec{v}_p}{d\tau} = \frac{1}{F_N} \left\{ \frac{1}{v_s} (\vec{v}_a - \vec{v}_p) \frac{B_{N,R_N,s}}{B_{N,s} R_N} - \vec{k} \right\} \quad (4)$$

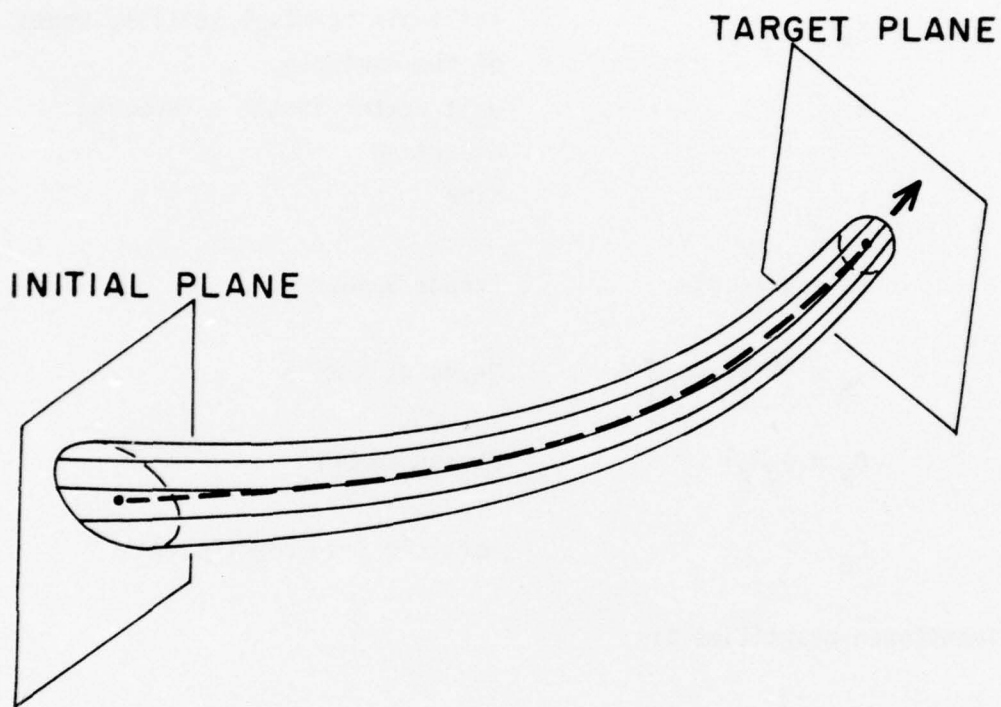


Figure 2. Perspective view of a particle flux tube.

Non-dimensioned quantities are:

\vec{v}_p, \vec{v}_a	particle and air velocities
v_s	still-air terminal settling speed of the particle
\vec{k}	unit vector in the z (upward) direction
τ	time
$F_N = V^2/(Lg)$	Froude Number
$R_N = \frac{\rho \delta}{\eta} \left \vec{v}_a - \vec{v}_p \right V$	Reynolds Number
$B_N = C_D R_N^2$	Davies Number
C_D	particle drag coefficient

Dimensioned quantities are:

δ	particle dimension
ρ	air density
η	air viscosity
g	gravity acceleration constant
V	freestream airspeed
L	a characteristic dimension of the fuselage

Here length is normalized by L , velocity by V and time by L/V . $R_{N,s}$ and $B_{N,s}$ are for still-air, terminal settling of the particles.

Starting at the initial plane, eq. (4) is integrated

with respect to time in three-dimensional space via the code DVDO of Krogh⁽³⁾ till the target plane is reached. The method used to compute \vec{v}_a at each time step is described next, and then drag coefficients are discussed.

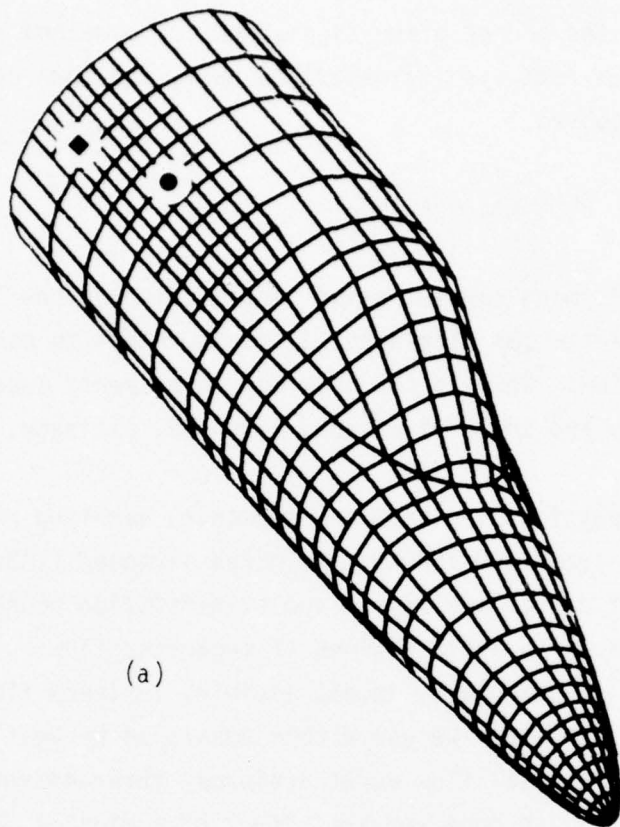
THREE-DIMENSIONAL FLOW CALCULATION

In performing concentration factor calculations for sampling sites on particular airplanes, it is important to use three-dimensional airflow. This is the only way to properly account for: airplane geometry and angle-of-attack, airspeed, altitude, and particle settling.

Cloud physics airplanes are subsonic, sampling runs being made typically between 100-150 kts indicated airspeed (IAS). Particle measurement points are beyond the skin-friction boundary layer, and should be placed to avoid regions of separated flow. Therefore, potential (i.e., frictionless, incompressible, laminar) flow calculations are quite adequate. We use a code developed by Hess and Smith^(4,5) for calculating potential flow about arbitrary three-dimensional bodies. The Hess-Smith code requires input of a digital description of the fuselage surface. This consists of the coordinates of the corner points of a large number of contiguous, plane, quadrilaterals. An example of the digital description of a fuselage is shown in Fig. 3.

Accuracy of the flow calculations has been checked with excellent results by Hess and Smith⁽⁴⁾ for many bodies for which analytical solutions are available. Norment and Zalosh⁽¹⁾ have compared computed trajectories around ellipsoids in analytical flow fields with similar trajectories in Hess-Smith flow fields, and they have compared current trajectory results with prior work; agreement is excellent.

-
3. F.T. Krogh, "Variable Order Integrators for Numerical Solutions of Ordinary Differential Equations," Jet Propulsion Lab Technology Utilization Document No. CP-2308 (November 1970).
 4. J.L. Hess and A.M.O. Smith, "Calculation of Non-Lifting Potential Flow About Arbitrary Three-Dimensional Bodies," McDonnell Douglas Report E.S. 40622 (15 March 1962). AD-282 255.
 5. J.L. Hess and A.M.O. Smith, "Calculation of Potential Flow About Arbitrary Bodies," Progress in Aeronautical Sciences, Vol. 8, edited by D. Kuchemann (Pergamon Press, New York, 1967).



(a)



(b)

Figure 3. Computer prepared plots of the digital description of the Learjet 36 fuselage: (a) Forward fuselage, (b) Complete fuselage. Instrument locations are: ASP ● , Replicator ■ , Snow Stick ▼ .

PARTICLE DRAG COEFFICIENT

Davies⁽⁶⁾ shows that still-air terminal settling of spheres can be generalized in terms of the dimensionless numbers $R_{N,S}$ and $B_{N,S}$. Over the range from the smallest spheres, which settle under viscous flow conditions and obey Stokes law, to spheres much larger than of interest here, and for any Newtonian fluid, a reproducible single-valued relationship between $R_{N,S}$ and $B_{N,S}$ exists. Furthermore, $B_{N,S}$ is independent of settling speed, being a function of fluid and sphere properties only; thus for given sphere and fluid, $R_{N,S}$ and hence V_S can be calculated. Polynomials by which $R_{N,S}$ can be computed as a function of $B_{N,S}$ were derived by Davies from a composite of many sets of experimental data.

Since the work of Davies, it has been found repeatedly that this treatment is applicable to particles of other shapes, providing settling is steady and particle orientation is stable.

For the trajectory calculations required here, the problem must be turned around. In addition to gravity settling, there is a particle velocity component (relative to air) caused by the disturbance of the passing airplane. At any time step in the numerical integration of eq. (4), $\vec{V}_a - \vec{V}_p$ (and hence R_N) is known, and B_N must be determined. For viscous motion (i.e., Stokes flow, where $R_N < 1$) $B_N = 24 R_N$ and eq. (4) can be integrated without question. However, for larger R_N the steady-state drag data determined experimentally for terminal settling must be used to compute accelerative particle motion.

Experimental measurements by Keim⁽⁷⁾ and a theoretical analysis by Crowe, et al.⁽⁸⁾ indicate that if the acceleration modulus,

-
6. C.N. Davies, "Definitive Equations for the Fluid Resistance of Spheres," Proc. Phys. Soc. (London) 57, 259-270 (1945).
 7. S.R. Keim, "Fluid Resistance to Cylinders in Accelerated Motion," J. Hydraulics Div., Proc. Amer. Soc. Civil Eng., 6, paper 1113 (1956).
 8. C.T. Crowe, J.A. Nicholls and R.B. Morrison, "Drag Coefficients of Inert and Burning Particles Accelerating in Gas Streams," Ninth Symp. (Int'l.) on Combustion, Academic Press, pp. 395-405 (1963).

$$A_N = \delta \left| \frac{dV}{dt} \right| / V_p^2 ,$$

is smaller than about 10^{-2} , steady-state drag coefficients can be used without significant error to compute accelerative motion. A_N has never been found to exceed 10^{-2} in our trajectory calculations.

For small water drops, which are spherical, the polynomial equations of Davies⁽⁶⁾ are used to compute V_s , while for larger, distorted drops, the equations of Foote and du Toit⁽⁹⁾ are used. To compute B_N from R_N , inverse polynomials have been developed, using the data set given by Davies for small drops and Gunn and Kinser⁽¹⁰⁾ for large drops.

Concentration factors also are calculated for a variety of ice crystal forms and for broad ranges of ice crystal sizes. Ice crystal drag and dimensional data are described in refs. 1 and 2.

-
9. G.B. Foote and P.S. du Toit, "Terminal Velocity of Raindrops Aloft," J. Appl. Meteor. 8, 249-253 (1969).
 10. R. Gunn and G.D. Kinser, "The Terminal Velocity of Fall for Water Droplets in Stagnant Air," J. Meteor. 6, 243-248 (1949).

LEARJET 36

INSTRUMENT LOCATIONS

A Learjet 36 airplane (Fig. 4) has been instrumented for cloud physics research by Meteorology Research, Inc. (MRI) as shown in Fig. 5. Instruments of interest here are:

- Total Water Content Indicator (TWCI)
- Particle Measuring Systems (PMS) 1-D Particle Spectrometers
- Snow Stick
- Formvar Replicator
- PMS Axial Scattering Probe (ASP)

Engineering drawings of surface contours of the fuselage were obtained from the Gates-Learjet Corp. The engineering coordinate system is as follows for this airplane:

- FS Along the fuselage axis, increasing in the aftward direction, with origin 86.75" forward of the nose tip.
- BL Horizontal direction perpendicular to the fuselage axis with origin at the axis.
- WL Vertical direction, increasing upward, with origin at the lowermost level of the fuselage.

For the calculations reported here, the origin is shifted to the nose tip (actually to the center of the TWCI orifice) and all coordinates are normalized by dividing by the radius of the upper portion of the cylindrical fuselage section (32"). Coordinates of



Figure 4. Learjet 36. Length - 48.7 ft, Wingspan - 39.5 ft, fuselage radius - 32 in.
See Fig. 5 for instrument locations.

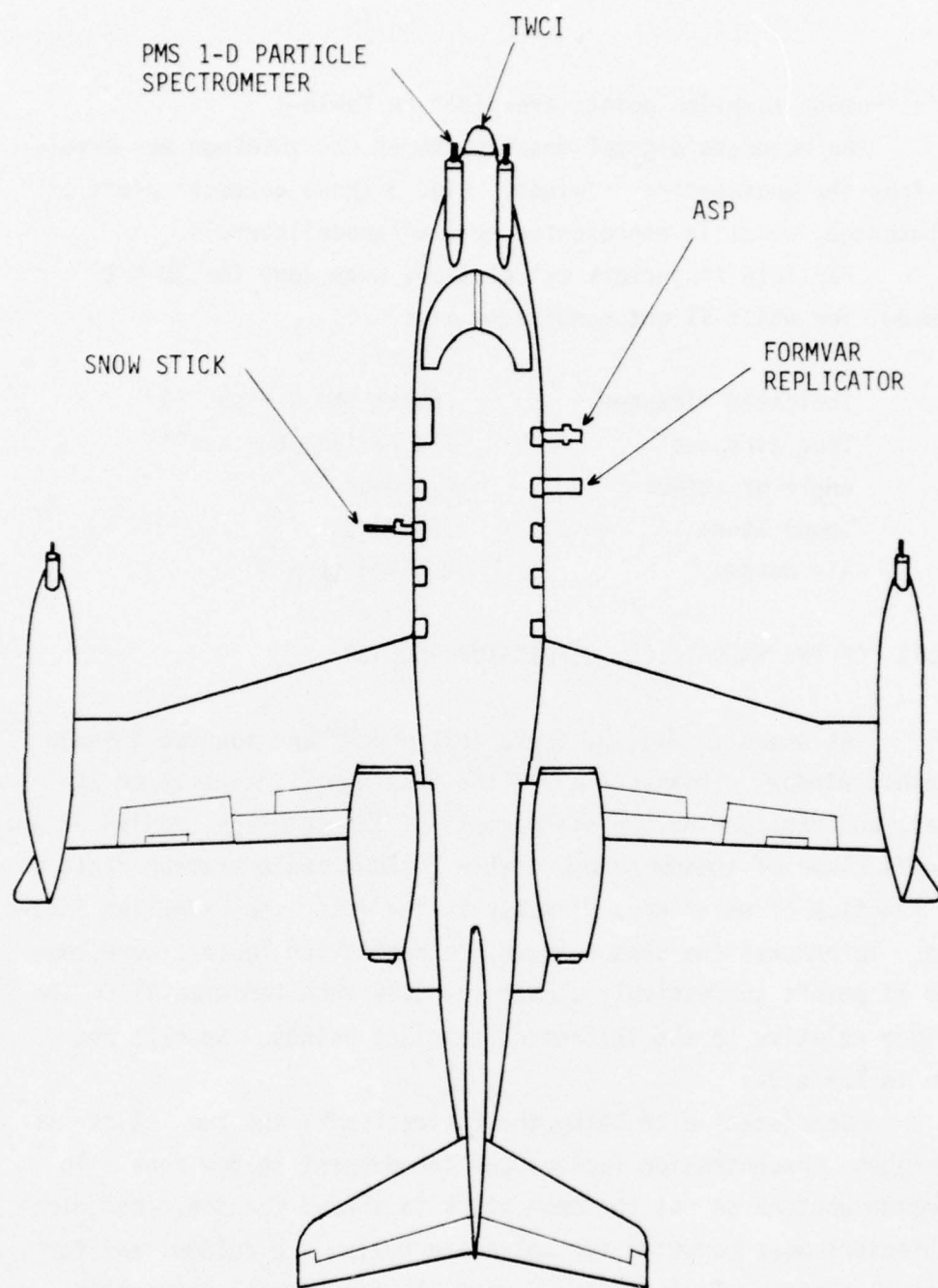


Figure 5. Learjet 36 with instruments mounted.

the instrument sampling points are given in Table 1.

An accurate digital description of the fuselage was developed from the engineering drawings. Fig. 3 shows computer plots of the fuselage, which is represented by 1104 quadrilaterals.

Particle trajectory calculations were done for 30 kft altitude, for which flight conditions are:

Indicated airspeed	165 kt (84.9 m sec^{-1})
True airspeed	270 kt (138.8 m sec^{-1})
Angle of attack	4.5 deg
Temperature	228.8° K
Air density	$0.45904 \text{ kg m}^{-3}$

RESULTS FOR THE SNOW STICK, REPLICATOR AND ASP

As shown in Fig. 5, these instruments are mounted through the cabin windows. Distances from the fuselage skin are 13 or 14 inches, and considering the slenderness of the fuselage (radius 32 in.) are well clear of shadow zones. Table 2 shows concentration factors as a function of water drop diameter at the instrument sampling locations. To bracket the shadow zones, concentration factors were computed at points successively closer (by 2.54 inch increments) to the fuselage relative to the instrument sampling points. Results are shown in Table 3.

Consistent with being the furthest aft, the snow stick has the highest concentration factors and the deepest shadow zone. To determine whether or not the snow stick is shaded for ice, concentration factors were computed for solid and hollow ice columns and for hexagonal plates. Tables 4 and 5 give the ice crystal properties and Table 6 gives the concentration factor results. No shadowing is indicated.

TABLE 1

COORDINATES OF INSTRUMENT SAMPLING POINTS ON THE LEARJET 36*

Instrument	Distance from Fuselage (inches)	Engineering System (inches)			System Used in These Calculations (dimensionless)			Computed Air Speed Ratio (Eq. (2)) V/V_t
		FS	BS	WL	x	y	z	
TWCI	0	86.8	0	9.2	0	0	0	20.0
PMS 1-D Probes	8	104.8	6.75	29.2	0.5625	0.2109	0.625	1.076
Snow Stick	13	287.3	44.4	38.4	6.266	1.386	0.914	0.984
Replicator	13	260.9	44.1	37.4	5.441	1.377	0.882	0.976
ASP	14	~239.4	42.5	45.0	~4.770	1.329	1.120	0.961

* From measurements made on the airplane by Larry Jahnsen of MRI.

TABLE 2

WATER DROP CONCENTRATION FACTORS

AT THE LEARJET 36 SNOW STICK, FORMVAR REPLICATOR and ASP

Water Drop Diameter (μm)	CONCENTRATION FACTOR, C_F		
	<u>Snow Stick</u>	<u>Replicator</u>	<u>ASP</u>
50	1.148	1.155	1.151
80	1.203	1.173	1.136
100	1.194	1.153	1.116
300	1.046	1.032	1.023
500	0.987	0.988	0.998
800	0.984	0.985	0.987

TABLE 3

SHADOW ZONE BRACKETING FOR INSTRUMENTS ON THE LEARJET 36

Instrument	Inboard * Increment (inches)	Distance from Fuselage (inches)	Concentration Factor ** for Water Drops of Diameter:			
			50 μ m	80 μ m	100 μ m	150 μ m
Snow Stick	0	13.0	1.15	1.20	1.19	
	2.54	10.5	1.25	1.40	1.36	1.21
	5.08	7.9		S	S	S
Replicator	0	13.0	1.16	1.17	1.15	
	2.54	10.5	1.28	1.34	1.27	
	5.08	7.9			S	
ASP	0	14.0				
	2.54	11.5	1.21	1.25	1.16	1.10
	5.08	8.9	1.37	1.32	1.25	1.15
	7.62	6.4		S	1.46	

* Relative to the center of the instrument sampling region.

** S entries denote that the sampling point lies inside the shadow zone.

TABLE 4

PROPERTIES OF COLUMNAR ICE CRYSTALS

Length, ℓ (μm)	Width, δ (μm)	δ/ℓ	Solid Columns*		Hollow Columns*	
			Mass (μg)	Diameter of water drop of equal mass (μm)	Mass (μg)	Diameter of water drop of equal mass (μm)
20	11.559	.578	.001215	13.2	.0006248	10.6
30	17.441	.581	.004149	19.9	.002134	16.0
50	35.8	.715	.0291	38.1	.0149	30.6
100	68.3	.683	.212	74.0	.1091	59.3
300	117.0	.390	1.87	152.8	.960	122.4
500	144.5	.289	4.75	208.5	2.441	167.1
1000	197.3	.197	17.7	323.3	9.100	259.0
3000	310.9	.104	131.9	631.5	67.82	506.0

* Solid column density is taken to be 0.7 g/cm^3 , and hollow column density is taken to be 0.36 g/cm^3 .

TABLE 5

PROPERTIES OF HEXAGONAL PLATE (P1a) ICE CRYSTALS

Diameter (μm)	Thickness (μm)	Mass (μg)	Diameter of Water Drop of Equal Mass (μm)	Density (kg/m^3)
10	5.68	$\sim 2.582 \times 10^{-4}$	~ 7.9	$\sim 700.$
30	9.30	$\sim 3.591 \times 10^{-3}$	~ 19	~ 660.6
50	11.70	$\sim 9.203 \times 10^{-3}$	~ 26	~ 484.0
100	15.97	$\sim 3.351 \times 10^{-2}$	~ 40	~ 323.0
300	26.16	0.4779	97	312.5
500	32.90	2.145	160	401.5
1000	44.91	20.22	338	693.1

TABLE 6

ICE CONCENTRATION FACTORS AT THE LEARJET 36 SNOW STICK

a. COLUMNS

<u>Length</u> <u>(μm)</u>	Concentration Factor, C_F	
	<u>Solid</u>	<u>Hollow</u>
20		1.032
30	1.048	1.039
50	1.089	1.060
100	1.181	1.116
300	1.241	1.211
500	1.221	1.242
1000	1.164	1.251
3000	1.086	1.178

b. HEXAGONAL PLATES

<u>Diameter</u> <u>(μm)</u>	<u>C_F</u>
30	1.050
50	1.053
100	1.062
300	1.122
500	1.190
1000	1.262

PARTICLE TRAJECTORY ANGLE AT THE 1-D PARTICLE SPECTROMETERS

As shown in Fig. 5, a pair of PMS particle spectrometers are mounted above the fuselage nose. The sampling volumes are 18" aft of the nose tip and are slightly more than 8" from the nose surface.

We expected no significant concentration distortion and found none, but there was interest in determining trajectory angles relative to the horizontal at the sampling points. Figure 6 shows a short segment of trajectory for 300 μ m diameter water drops to one of the spectrometers. The airplane axis is tilted at 4.5° . The trajectory is almost horizontal, being tilted in the same sense as the airplane axis at an angle less than 0.5° at the sampling point.

TOTAL WATER CONTENT INDICATOR

Instrument Description

The intake orifice of the TWCI consists of a 2 inch diameter hole in the nose tip of the fuselage. Intake air velocity is about 30 ft sec^{-1} , but will vary somewhat with flight conditions. For the calculations reported here, we have used an intake of 5% of the free-stream airspeed, which corresponds to 23 ft sec^{-1} at 30 kft altitude. A 6° angle of attack was used for the TWCI calculations.*

As illustrated by Fig. 3 the fuselage is represented by a large number (1104) of plane, contiguous quadrilaterals. Usually the fuselage symmetry is used so that only half of the total number of quadrilaterals need be specified. However, this requires that quadrilateral boundaries be defined along the symmetry plane, and unfortunately this plane bisects the TWCI orifice. Since flow accuracy is highest at quadrilateral centers and lowest at boundaries we considered it unwise to use the fuselage symmetry and have quadrilateral

*-----

At the time the TWCI calculations were done, the best information available indicated a 6° AOA, whereas a value of 4.5° should have been used to be consistent with the other calculations reported here. However, we find that the AOA discrepancy produces negligible differences in the C_F results.

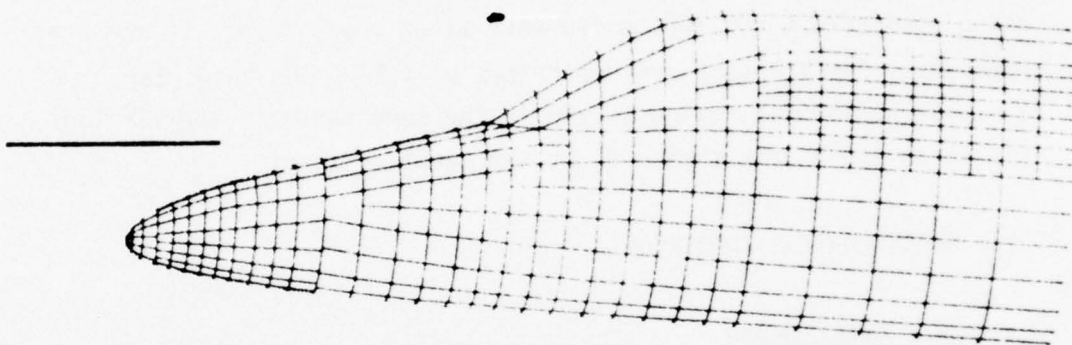


Figure 6. Computer prepared plot showing a segment of trajectory for a 300 μm diameter water drop to one of the PMS 1-D particle spectrometers. The airplane axis is inclined at 4.5 degrees to the horizontal.

boundaries running through the orifice center. Thus a special version of the nose was developed for the TWCI study which does not use the symmetry. This version, shown in Fig 7a, allows the center of the orifice to coincide with a quadrilateral center. Since not using the symmetry essentially doubles the time for each air velocity computation, the fuselage is described faithfully only as far aft as the base of the cockpit windshield. Beyond this point the fuselage cross section is kept constant as shown in Fig. 7a. This description of the nose requires 471 quadrilaterals.

Figure 7b shows an enlargement of the nose tip of the Learjet fuselage. The 2 inch diameter orifice is represented by a plane consisting of 21 quadrilaterals. The airflow computer code was modified such that each of these 21 quadrilaterals "leaks" inward a specified portion (in this case 5%) of the freestream flow.

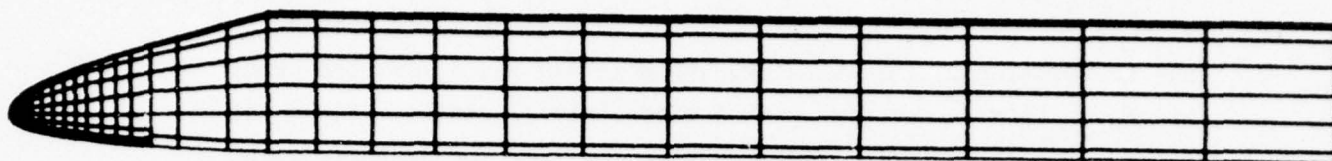
Flowfield Studies

Since we had not previously computed flow into and around an orifice, we performed a detailed study of the flow field in the vicinity of the nose tip. Calculations were done for zero, 5% and 100% intake relative to freestream airspeed. Flowfields in the fuselage symmetry plane (i.e., plane $y=0$) are shown in Fig. 8. (Note that there is little apparent difference between the zero intake and 5% intake cases.) Careful study of the numerical results indicate that the intake is accurate and uniform over essentially the entire surface of the orifice.

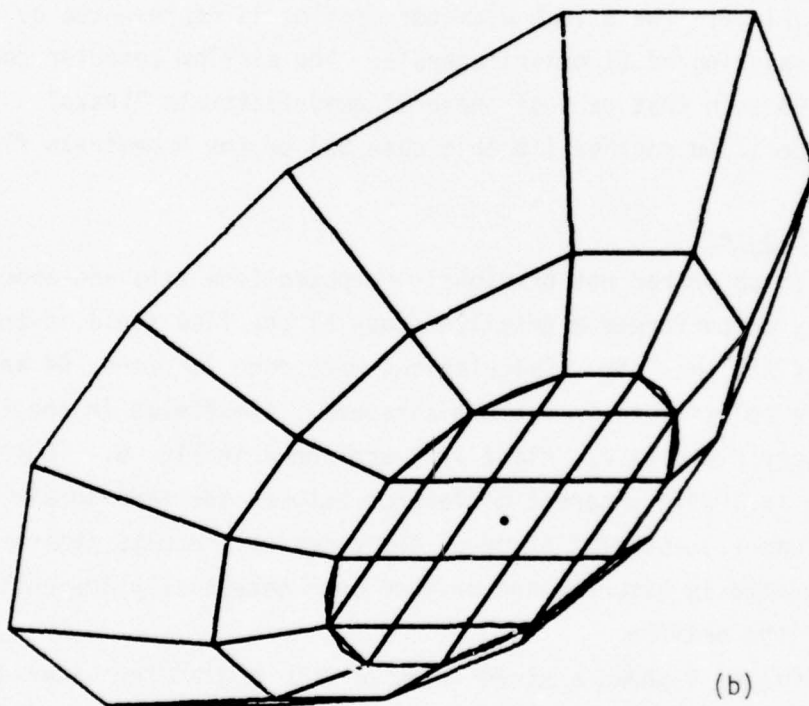
Figure 9 shows a stereo-view of 100 μm diameter water drops to the nose with 5% intake into the orifice. In the case of these particles the trajectories deviate little from straight lines.

Concentration Factors, Concentration Ratios and Concentration Correction Factors

Concentration factors were calculated in the usual manner



(a)



(b)

Figure 7. Special digital description of the Learjet 36 nose for the TWCI study: (a) Complete nose description (b) Enlargement of the nose tip. The center of the TWCI orifice is marked • .

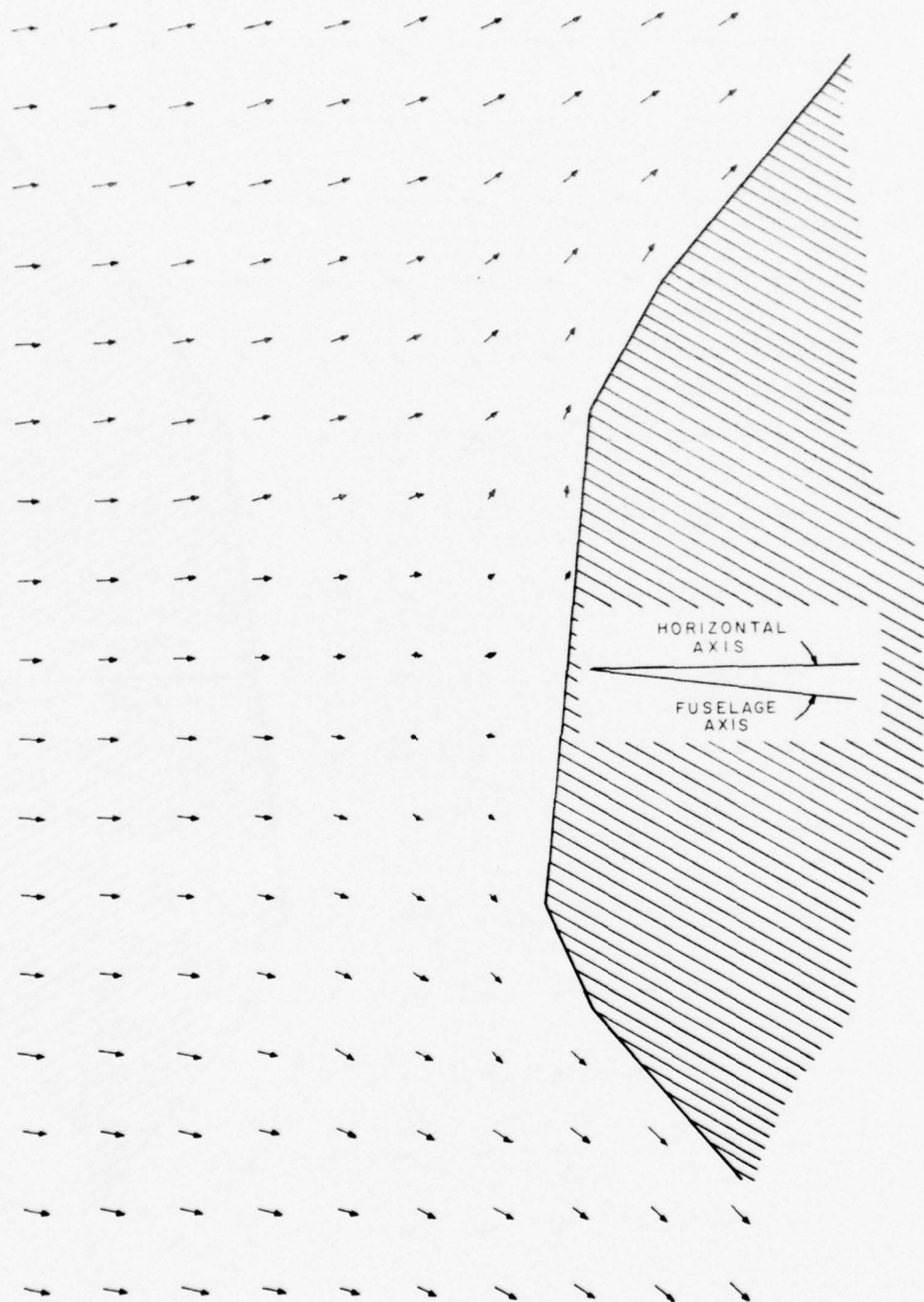


Figure 8a. Flowfield around the Learjet 36 nose tip in the plane $y=0$ for zero intake into the TWCI orifice.

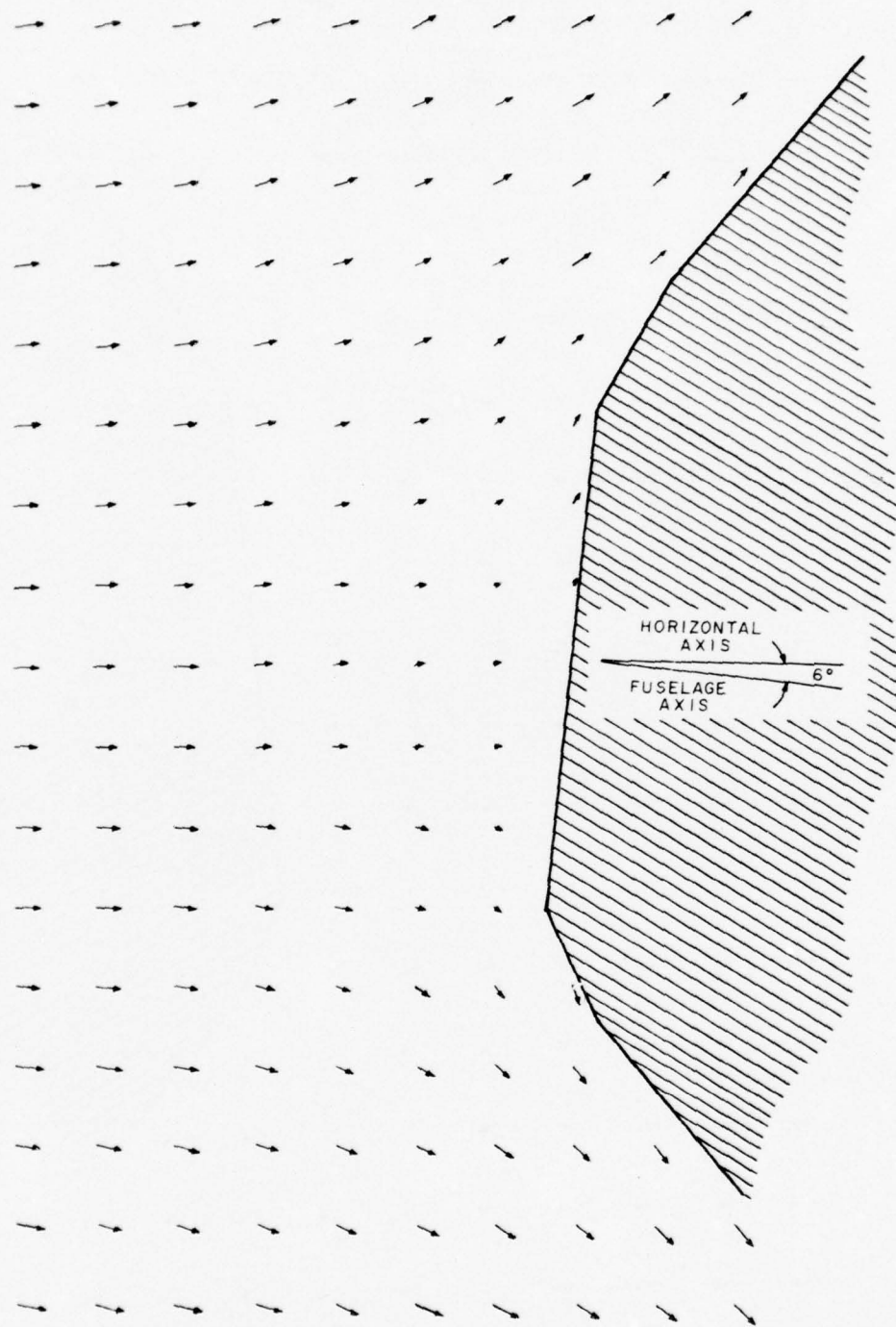


Figure 8b. Flowfield around the Learjet 36 nose tip in the plane $y=0$ for intake of 5% of the freestream flow into the TWCI orifice.

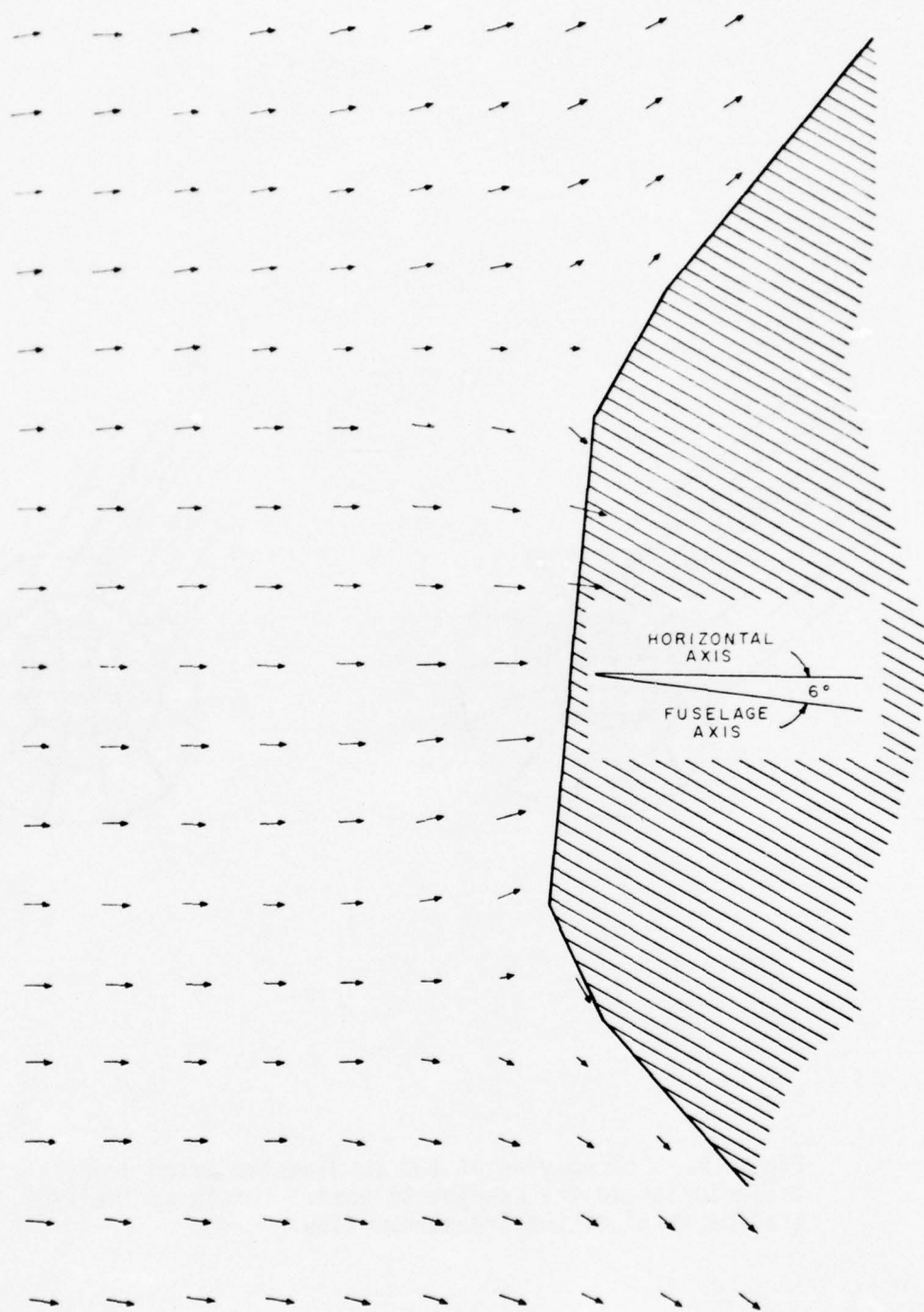


Figure 8c. Flowfield around the Learjet 36 nose tip in the plane $y=0$ for intake of 100% of the freestream flow into the TWCI orifice.

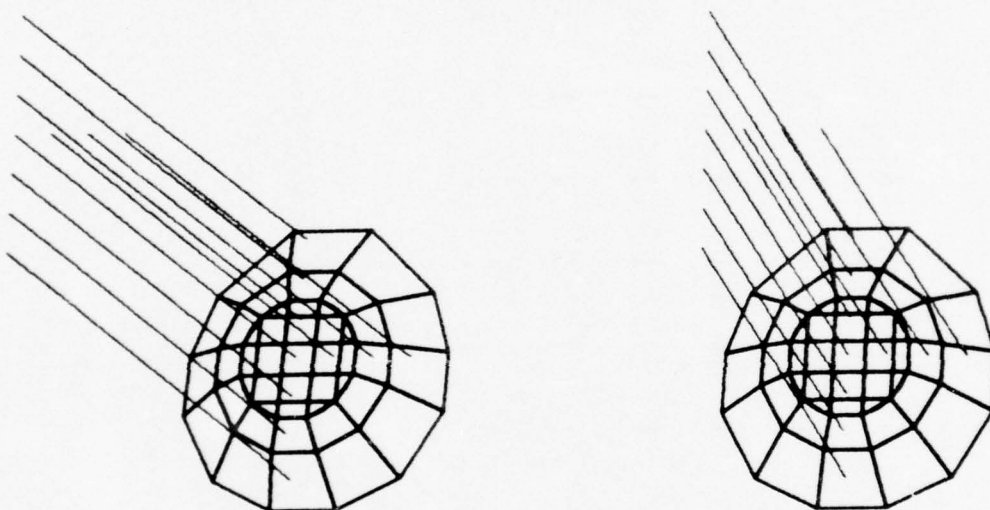


Figure 9. Stereo view of 100 µm diameter water drop trajectories to the Learjet 36 nose. Intake of the TWCI orifice is 5% of the freestream flow.

except that the target plane (Fig. 2) was constrained to lie parallel to the orifice plane at a distance 1.6 mm upstream from it. Particle flux tubes were centered at the orifice center.

To explore the effect of flux tube radius on water drop concentration factor results, calculations were done for target plane flux tube radii of 0.5, 0.8 and 0.9 inch. (The orifice radius is 1 inch.) Negligible differences in results were obtained over a drop diameter range of 50 to 800 μm . All results reported below are for target plane flux tube radii of 0.9 inch.

Concentration factors, C_F , for water drops are given in Table 7.* Figure 10 shows a flux tube of 10 μm diameter waterdrops to the TWCI. As seen in the figure, the tube flares open as it approaches the TWCI; therefore we have $A_t > A$, and $C_F < 1$ (see eq. (3)). Figure 11 shows that otherwise there is little flux tube distortion.

Concentration factor does not provide an approximation to particle concentration distortion in the same way that it does for the more conventional cases involving sampling instruments protruding from the fuselage aft of the nose. This is because the TWCI orifice is very nearly a stagnation area, and we cannot assume, as usual, that the particle velocity is essentially the same as the air velocity. The ratio of particle concentration at the TWCI orifice to the free-stream concentration is

$$C_M = C_F V/V_{p,t} \quad (5)$$

where $V_{p,t}$ is the particle speed into the orifice and V is freestream airspeed. Table 7 also contains the ratio $V/V_{p,t}$ and C_M . Except

* Water drop concentration factors also were calculated for zero intake into the TWCI. C_F values are not significantly different from those given in Table 7.

TABLE 7

WATER DROP CONCENTRATION RATIOS AT THE LEARJET 36 TWC1 FOR 5% AIR INTAKE

Water Drop Diameter (μm)	Mass (μg)	C_F	$V/V_{p,t}^*$	C_M	C_F^{-1}
10	5.236×10^{-4}	.358	3.978	1.426	2.790
30	.01414	.742	1.488	1.105	1.347
50	.06545	.853	1.242	1.059	1.172
100	.5236	.932	1.096	1.021	1.073
300	14.14	.973	1.028	1.000	1.028
500	65.45	.979	1.019	0.998	1.021
800	268.1	.983	1.014	0.997	1.017

* $V/V_{p,t}$ is computed at a point 1.6 mm upstream of the orifice center, which is the point of closest approach of the particles. At this point the air speed ratio is 10.3, which can be compared with the value 20 in the orifice plane.

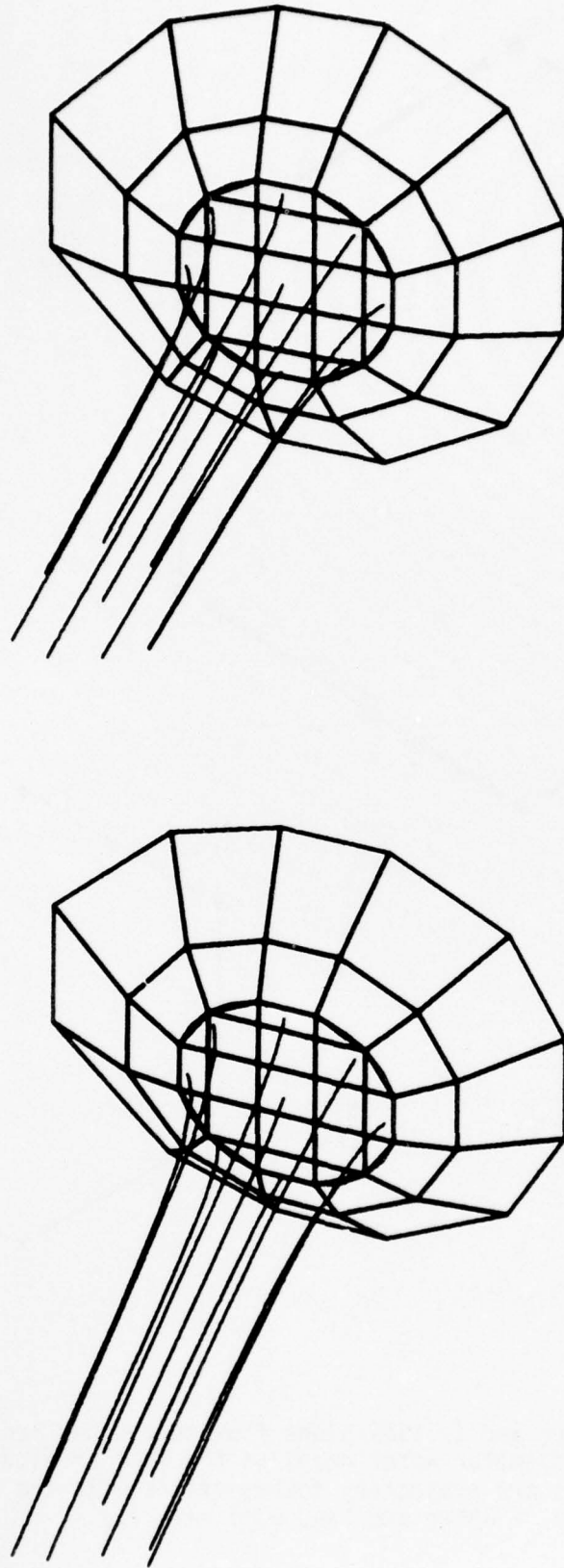


Figure 10. Stereo view of a flux tube of 10 μm diameter water drops to the Learjet 36 TWCI orifice.

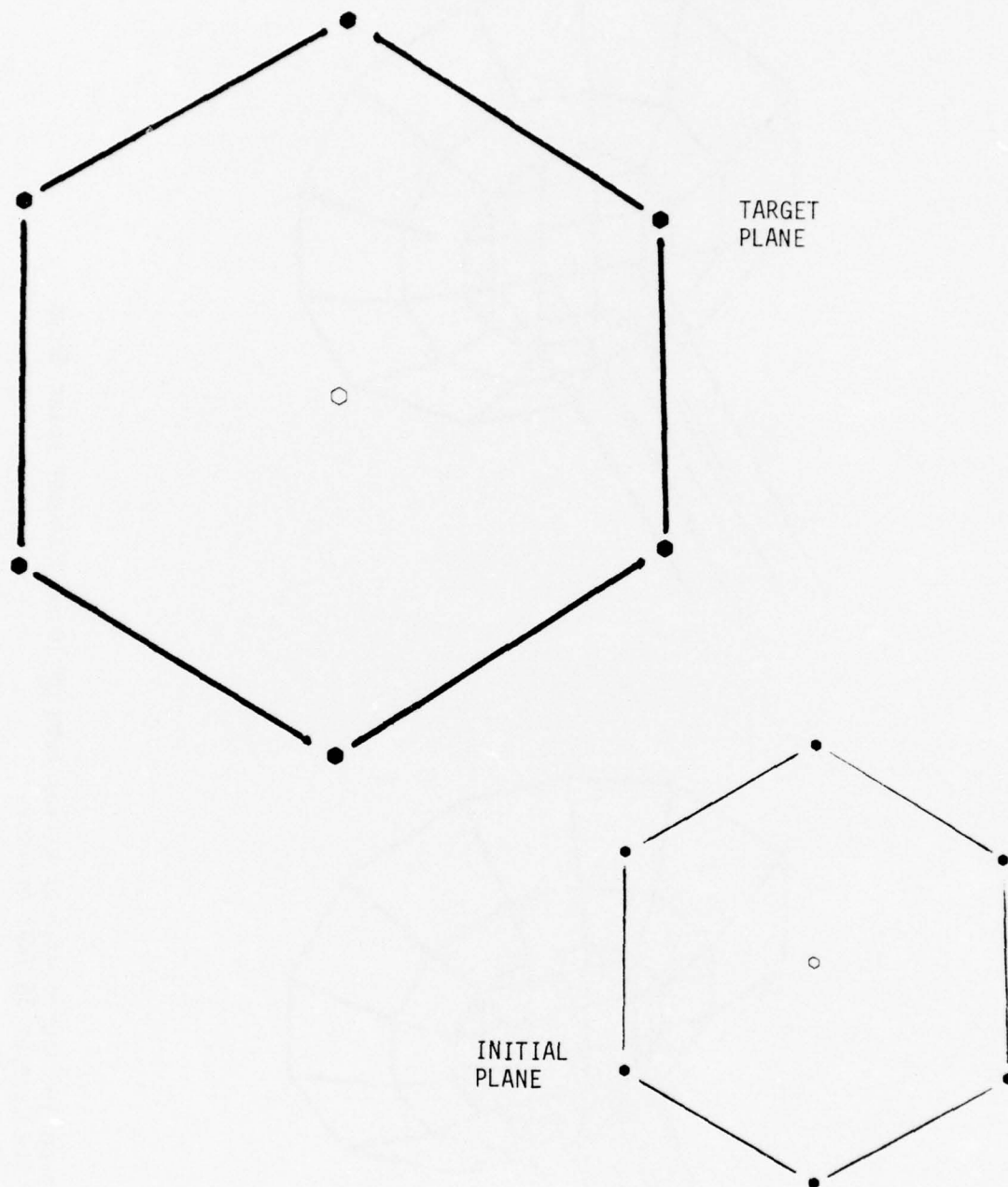


Figure 11. Target and initial plane flux tube cross sections for $10\text{ }\mu\text{m}$ diameter water drops to the TWCI orifice. The marked points are trajectory intersections with the planes. (Cf. Fig. 2 above and Fig. 8 of ref. 1.)

for the smallest water drops there is little concentration distortion at the orifice. Obviously, this comes about because flux decrease is compensated by concentration buildup in the stagnation region.

Though particle concentrations at the TWCI orifice are nearly the same as freestream concentrations this does not mean that hydrometeor concentrations measured by the TWCI are free of distortion. The TWCI measures the throughput rate of bulk particle mass, \dot{m} . This is

$$\dot{m} = C_t A_o V_{p,t} \quad (6)$$

where C_t is the actual concentration at the orifice, and A_o is orifice area. From the definition of concentration ratio, the freestream concentration, C , is

$$C = \frac{\dot{m}}{C_M A_o V_{p,t}}$$

and substitution of eq. (5) into this gives

$$C = \frac{\dot{m}}{A_o V} \frac{1}{C_F} \quad (7)$$

Thus for the TWCI, distortion in hydrometeor concentration measurements is proportional to the reciprocal of concentration factor, and equation (7) should be used to compute freestream particle concentrations from the TWCI data.

Concentration factor calculations also were done for solid and hollow ice columns, hexagonal plates, plane dendrites and aggregates of unrimed radiating assemblages of plates, side planes, bullets and columns. Properties of the ice hydrometeors are given in Tables 4,5,8,9. (Explanations of these tables are in ref. 2) Results are given in Tables 10-13 and Fig. 12.

TABLE 8
PROPERTIES OF PLANE DENDRITIC (P1e) ICE CRYSTALS

<u>Dendrite Diameter (μm)</u>	<u>Thickness (μm)</u>	<u>Mass (μg)</u>	<u>Diameter Of Water Drop Of Equivalent Mass (μm)</u>	<u>Equivalent Disc Density (kg/m^3)</u>	<u>Diameter (μm)</u>
500	29.16	0.7356	112	334	341.0
600	31.24	1.0981	128	357	389.4
800	34.82	2.1850	161	402	490.3
1000	37.87	3.6484	191	450	574.1
1500	44.13	8.2800	251	556	720.8
1800	47.27	11.494	280	607	785.4
2500	53.50	~ 21.129	~ 343	~ 712	924.1

TABLE 9
PROPERTIES OF AGGREGATES OF UNRIMED RADIATING ASSEMBLAGES OF
PLATES, SIDE PLANES, BULLETS AND COLUMNS

<u>Dimension (μm)</u>	<u>Mass (μg)</u>	<u>Density (kg/m^3)</u>	<u>Diameter of Water Drop of Equivalent Mass (μm)</u>
300	3.756	265.7	193
500	9.914	151.5	266
800	24.21	90.3	359
1000	37.0	70.7	413
2000	138.1	33.0	641
3000	298.3	21.1	829

TABLE 10
ICE COLUMN CONCENTRATION RATIOS AT THE LEARJET TWC1

Column Length (μm)	Solid Columns				Hollow Columns			
	C_F	$V/V_{p,t}$	C_M	C_F^{-1}	C_F	$V/V_{p,t}$	C_M	C_F^{-1}
20	.373	3.876	1.446	2.678	.238	6.349	1.513	4.195
30	.535	2.427	1.297	1.870	.385	3.723	1.435	2.595
50	.742	1.543	1.145	1.347	.622	1.992	1.240	1.607
100	.860	1.261	1.084	1.163	.780	1.471	1.146	1.283
300	.919	1.139	1.047	1.088	.869	1.253	1.089	1.151
500	.935	1.107	1.035	1.070	.895	1.196	1.071	1.118
1000	.951	1.074	1.022	1.051	.923	1.135	1.048	1.084

* See Table 4 for ice column properties.

** See footnote in Table 7.

TABLE 11

HEXAGONAL PLATE (Pla) CONCENTRATION RATIOS AT THE LEARJET 36 TWC1

Plate Diameter* (μm)	C_F	$V/V_{p,t}^{**}$	C_M	C_F^{-1}
10	.401	3.448	1.383	2.492
30	.533	2.433	1.299	1.875
50	.560	2.320	1.297	1.787
100	.601	2.137	1.283	1.665
300	.761	1.558	1.185	1.314
500	.836	1.348	1.128	1.196
1000	.919	1.151	1.057	1.088

* See Table 5 for hexagonal plate properties.

** See footnote in Table 7.

TABLE 12

PLANE DENDRITE (Ple) CONCENTRATION RATIOS AT THE LEARJET 36 TWC1

Dendrite * Diameter (μm)	C_F	$V/V_{p,t}^{**}$	C_M	C_F^{-1}
500	.789	1.472	1.161	1.267
600	.810	1.413	1.145	1.234
800	.842	1.330	1.120	1.187
1000	.866	1.273	1.102	1.155
1500	.900	1.190	1.071	1.111
1800	.912	1.164	1.062	1.096
2500	.930	1.125	1.046	1.076

* See Table 8 for plane dendrite crystal properties.

** See footnote in Table 7.

TABLE 13

CRYSTAL AGGREGATE CONCENTRATION RATIOS AT THE LEARJET 36 TWC1

Aggregate * Dimension (μm)	C_F	$V/V_{p,t}^{**}$	C_M	C_F^{-1}
300	.951	1.058	1.006	1.052
500	.959	1.046	1.002	1.043
1000	.967	1.033	.999	1.034
3000	.975	1.021	.996	1.026

* See Table 9 for crystal aggregate properties.

** See footnote in Table 7.

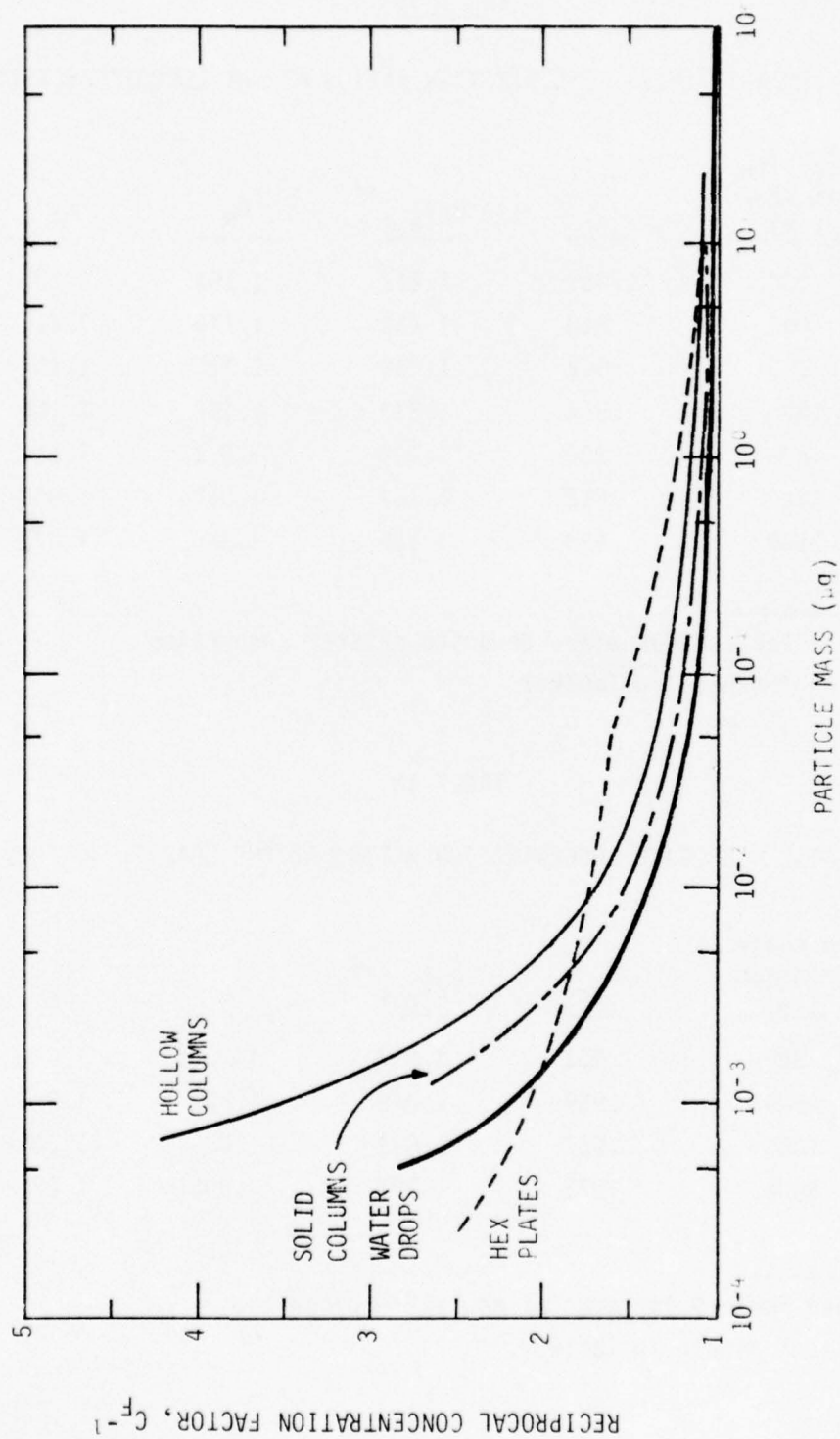


Figure 12. Reciprocal concentration factor vs. particle mass for various hydrometeors as collected by the Learjet 36 TWC. Tables 4, 5, 8, 9 list particle dimensions as a function of mass.

C_M values indicate that ice particle concentrations at the orifice also are not much different from freestream values. However, with exceptions of the largest hydrometeors of all types and ice crystal aggregates of all sizes, C_F values are substantially less than one. This means that corrections applied to the TWCI data via the reciprocal concentration factor in eq. (7) usually are very significant.

GENERALIZATION OF THE CONCENTRATION FACTOR METHOD FOR FUSELAGE-MOUNTED INSTRUMENTS

INTRODUCTION

The concentration factor calculation method described above and in refs.1 and 2 is designed to be specific with respect to airplane, sampling site and flight conditions. Its application requires development of a detailed digital description of the airplane fuselage followed by a rather demanding computational effort on a large computer. Frequently it is desirable to make a preliminary estimate of the suitability of a sampling location without resorting to this detailed analysis. To accomodate such need, the analysis described below was done. It results in a graph that can be used to roughly bracket the edge of the shadow zone for sampling points near any fuselage.

CONCENTRATION FACTOR RESULTS FOR POTENTIAL FLOW AROUND AN ISOLATED POINT SOURCE

A single point source in a potential flow field affords a simple, easily computed approximation to flow around an airplane fuselage. Thus, this approximation was used for the extensive concentration factor calculations required for the generalization. Figs. 13-15 show water drop trajectories around two point source bodies. The smallest drops ($10\text{ }\mu\text{m}$ diameter) follow the streamflow very closely and Fig. 13 essentially shows air streamlines. Fig. 14 illustrates the increase with distance aft of the depth of the shadow zone for $100\text{ }\mu\text{m}$ diameter drops, and Fig. 15 shows the relatively unaffected trajectories of large drops. The point source body definition and the flow field equations are given in the Appendix.

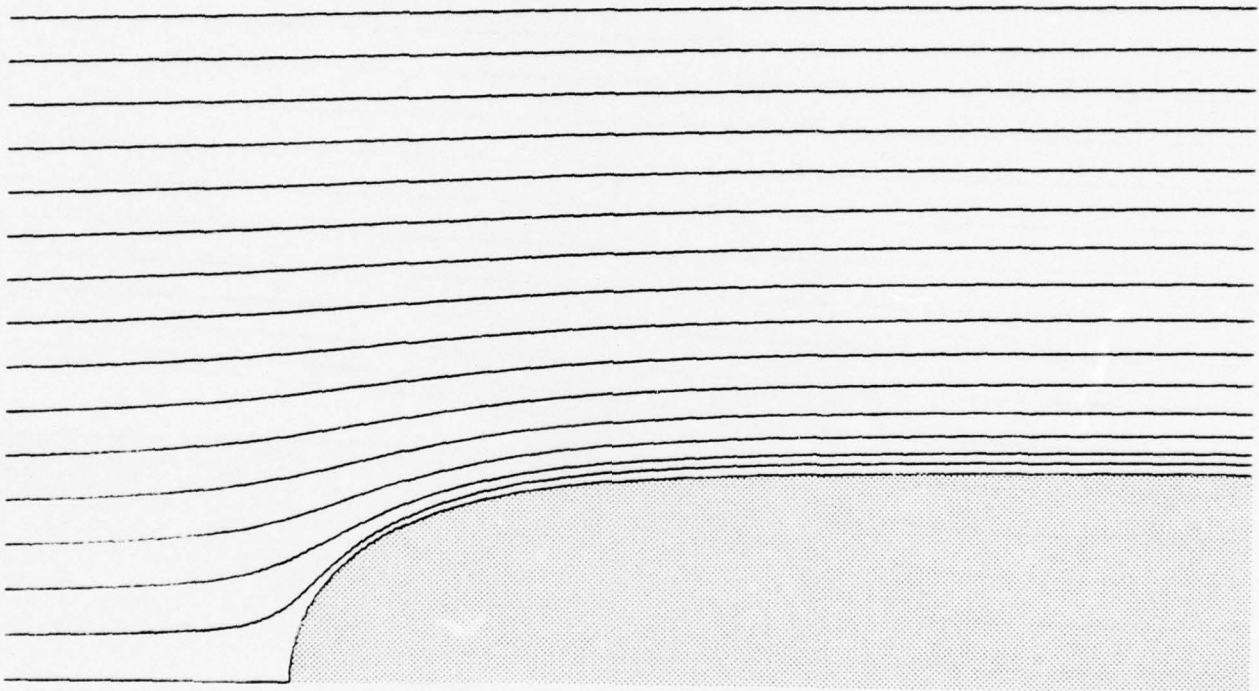


Figure 13. Trajectories of 10 μm diameter water drops in potential airflow around a single point source which simulates a fuselage of radius 0.8 m with velocity 130 m sec^{-1} at 20 kft altitude. These trajectories virtually coincide with airflow streamlines.

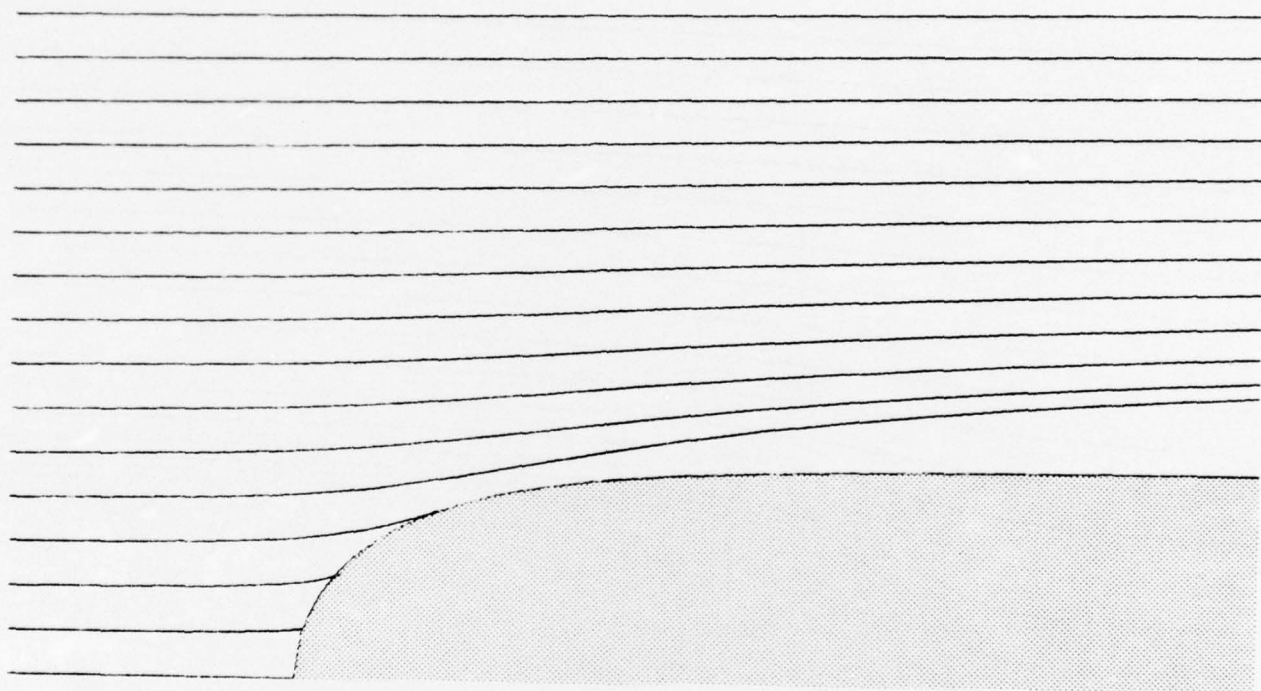


Figure 14a. Trajectories of 100 μm diameter water drops through a potential flow field around a single point source. These calculations simulate a fuselage of radius 0.8 m with velocity 130 m sec^{-1} at 20 kft altitude.

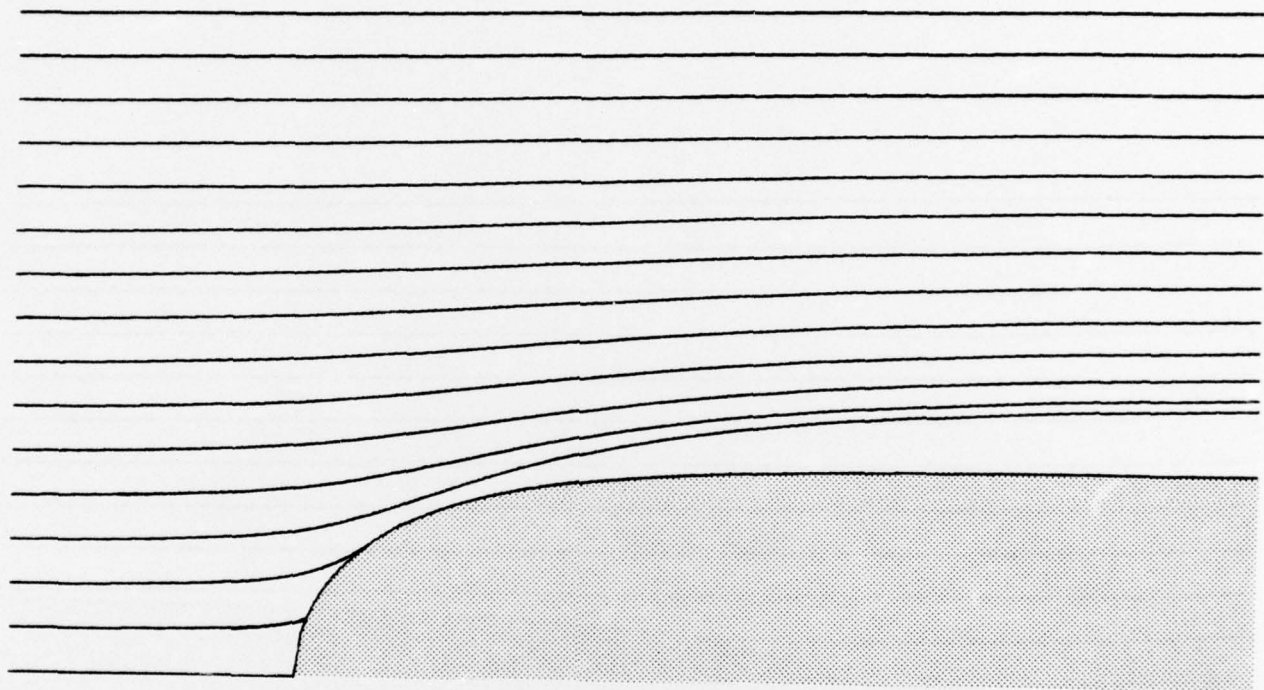


Figure 14b. Trajectories of 100 μm diameter water drops through a potential flow field around a single point source. These calculations simulate a fuselage of radius 2.0 m with velocity 130 m sec^{-1} at 20 kft altitude.

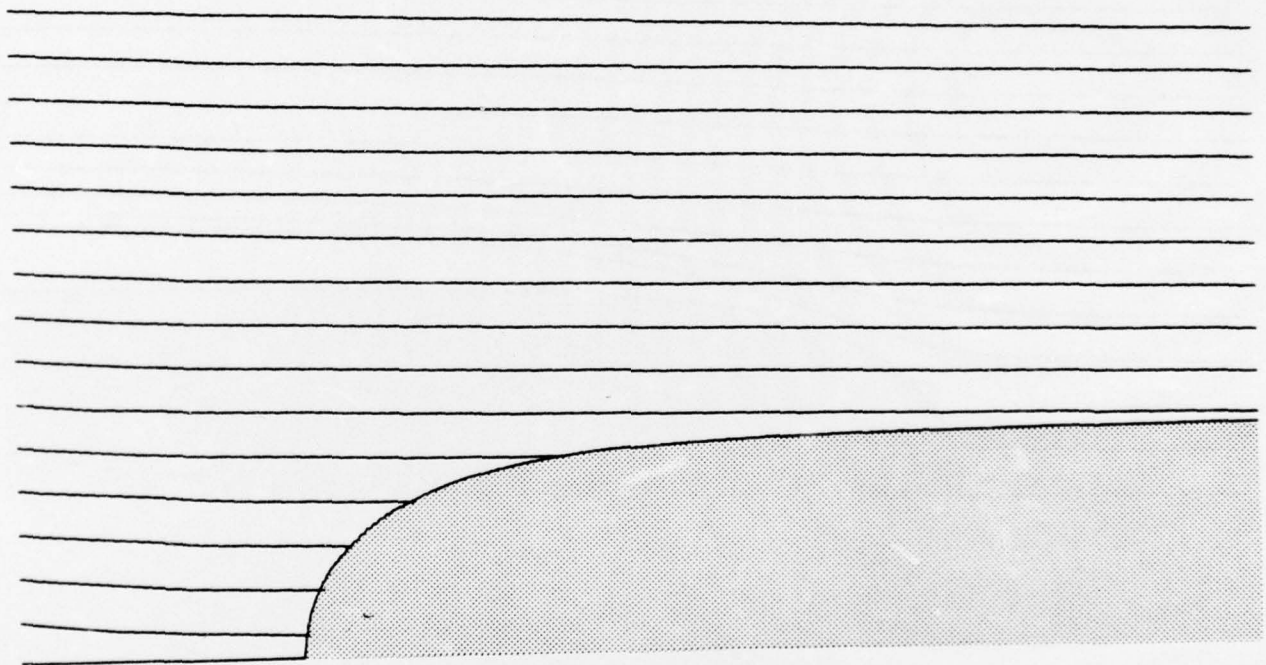


Figure 15. Trajectories of 1000 μm diameter water drops in potential airflow around a single point source. These calculations simulate a fuselage of radius 0.8 m with velocity 130 m sec^{-1} at 20 kft altitude. The tilt of the trajectories is caused by gravity settling.

Concentration factors were calculated such as to bracket the location of the shadow zone edge at nine x/D values ranging from 0.25 to 4.5. Here x is distance aft from the nose tip and D is the body diameter at $x = \infty$. Calculation geometry in the plane normal to the fuselage axis is shown in Fig. 16. The full three-dimensional concentration factor code for water drops was used.

The calculations were done for a standard-atmosphere altitude of 20 kft ($T = 248.6^\circ\text{K}$, $\rho = 0.653 \text{ kg m}^{-3}$), true airspeed of 130 m sec^{-1} and two fuselage radii: 0.8 m and 2.0 m. The smaller fuselage radius represents the smaller, more slender airplanes such as the Cessna Citation and Learjet. The larger radius represents large airplanes such as the Lockheed C130. The only significant difference between results for the two fuselages is that the concentration factor vs. drop diameter curves peak at about $50 \text{ }\mu\text{m}$ for the fuselage of smaller radius while they peak at about $80 \text{ }\mu\text{m}$ for the larger fuselage.

It is not possible to precisely determine the shadow zone edge via this method. This is because as the shadow zone is approached concentration factors increase sharply and numerical problems ensue. Thus, it is only possible to rather broadly bracket the shadow zone edge. The stippled region of Fig. 17 represents the bracketed region: $r-r_s$ values ($r-r_s$ corresponds to $y-y_s$ in Fig. 16) above the stippled area are clear of the shadow zone, values below the stippled area are within the shadow zone, and values within the stippled area may or may not be within the shadow zone but if not will have extremely high concentration distortion. The graph brackets the maxima of the concentration factor vs. water drop diameter curves. Distances are normalized by dividing by maximum body diameter, D .

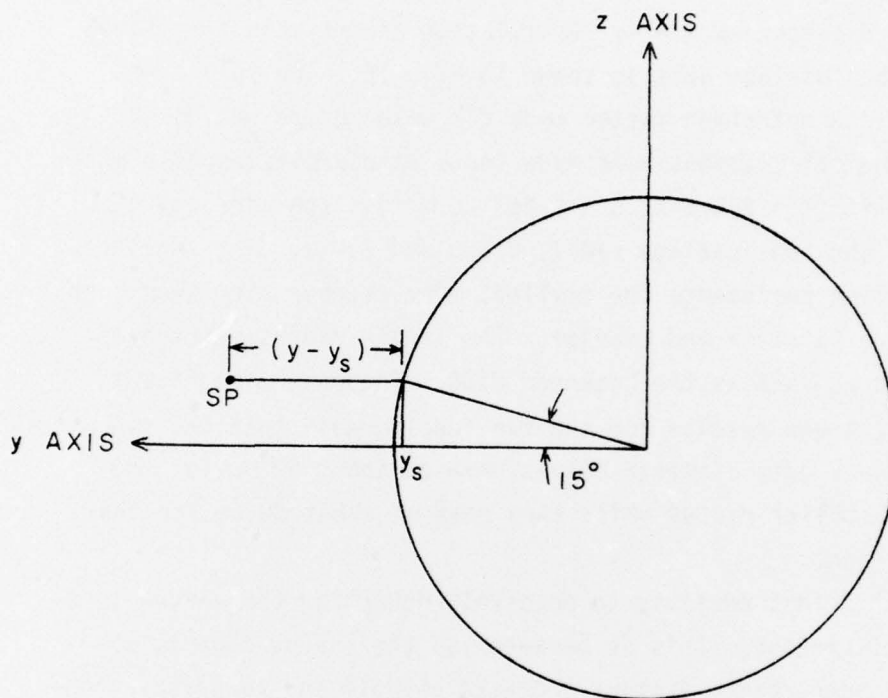


Figure 16. Cross section of simulated fuselage showing concentration factor calculation geometry used for the generalization calculations. SP is the sampling point. $y - y_s$ is the distance of the sampling point from the fuselage surface measured along the horizontal (y) axis. The z axis is vertical.

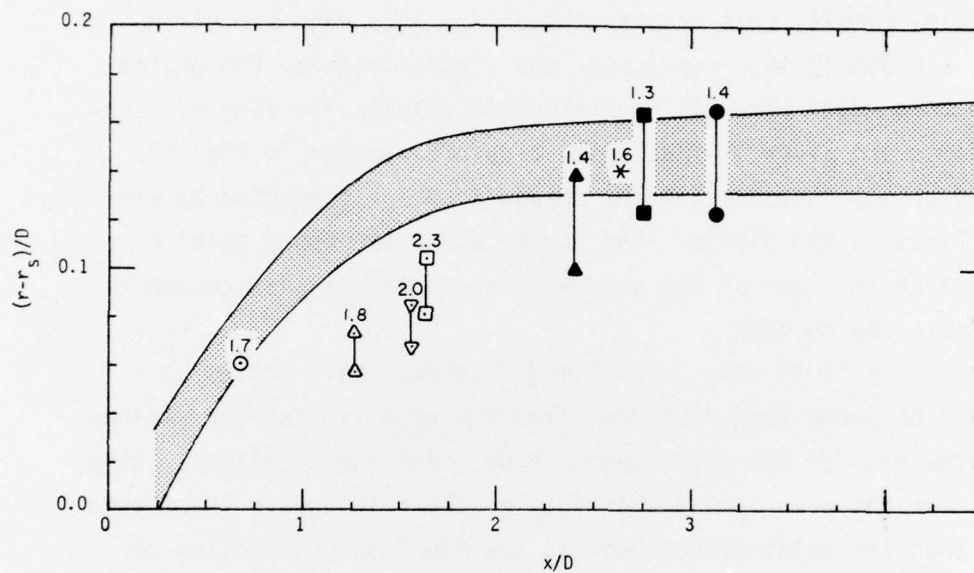


Figure 17. Summary of concentration factor results that bracket the shadow zone edge. x is distance aft from the nose tip. $r-r_s$ is distance from the fuselage surface. (For the flow around the point source body, $r-r_s = y-y_s$ as in Fig. 16.) D is maximum fuselage diameter. The stippled area brackets the shadow zone edge for flow around the point source body. Case study points are:

○ C130A Formvar Replicator	* Cessna Citation	{ PMS Precipitation Particle Spectrometer PMS Cloud Particle Spectrometer Snow Stick Formvar Replicator PMS Axial Scattering Probe
□ C130E Formvar Replicator	● Learjet 36	
△ C130B Lyman- α Total Water Probe	■ Learjet 36	
▽ C130B Foil Impactor	▲ Learjet 36	

See text for additional description.

COMPARISON WITH CASE STUDY RESULTS

Table 14 summarizes pertinent results of the case studies performed to date. Only for the Cessna Citation are the results for the instrument sampling points; for the other cases the results are for points closer to the fuselages along the instruments' axes. Where available, results that bracket the shadow zone edge are given. (For the C130A formvar replicator and Cessna Citation PMS probes, shadow zone edges were not bracketed and results for single, closest points are given.) These data also are plotted in Fig. 17. Plotted points that bracket the shadow zone are connected by vertical lines in the figure. The number above the upper point of a pair, which is clear of the shadow zone, is the largest concentration factor calculated.

Figure 18 shows normalized fuselage radii values as a function of normalized distances from the nose tip for the various airplanes and for the point source body. For the airplanes, the y_s values are for plan-view projections of the fuselages. The figure shows that the point source body is the bluffest obstruction to flow, but affords a reasonable approximation to the fuselage shapes with the exception of the Learjet.

That the point source body has the bluffest nose shape may at least partly explain why the case-study data all fall below that for the point source body for nose-mounted instruments ($x/D < 2$). The generalized and case-study data for instruments mounted on the sides of the cylindrical sections of fuselages ($x/D > 2$) agree very well.

Figure 17 should be considered as a preliminary result; more exhaustive calculations are necessary before the generalization can be considered to be complete. Nevertheless, the figure may be used to provide rough estimates of "safe" water drop sampling distances from fuselage surfaces.

TABLE 14

SUMMARY OF CASE-STUDY CONCENTRATION FACTOR RESULTS*

Airplane (Fuselage Diameter (m))	Instrument ⁺	x/D	$\frac{r-r_s}{D}$	C_F^{**}
C130A (4.32)	Formvar Replicator (Ref. 1)	0.682	0.061	1.7
C130E (4.32)	Formvar Replicator (Ref. 1)	1.627	0.104 0.081	2.5 S
C130B (4.32)	Lyman- α Total Water Probe (Ref. 11)	1.277	0.075 0.057	1.8 S
C130B (4.32)	Foil Impactor (Ref. 11)	1.562	0.085 0.068	2.0 S
Cessna Citation (1.61)	PMS Precipitation Particle Spectrometer (Ref. 1)	2.632	0.142	1.6
Cessna Citation (1.61)	PMS Cloud Particle Spectrometer (Ref. 1)	2.632	0.142	S
Learjet 36 (1.62)	Snow Stick	3.133	0.164 0.124	1.4 S
Learjet 36 (1.62)	Formvar Replicator	2.720	0.164 0.124	1.3 S
Learjet 36 (1.62)	PMS Axial Scattering Probe	2.384	0.140 0.100	1.3 S

* Concentration factors are peak values for water drops.

⁺ Only for the Cessna Citation PMS probes are the results given for the instrument sampling points. In all other cases the concentration factor results are for points closer to the fuselages along the instruments' axes.

^{**} S denotes that this sampling point lies inside the shadow zone.

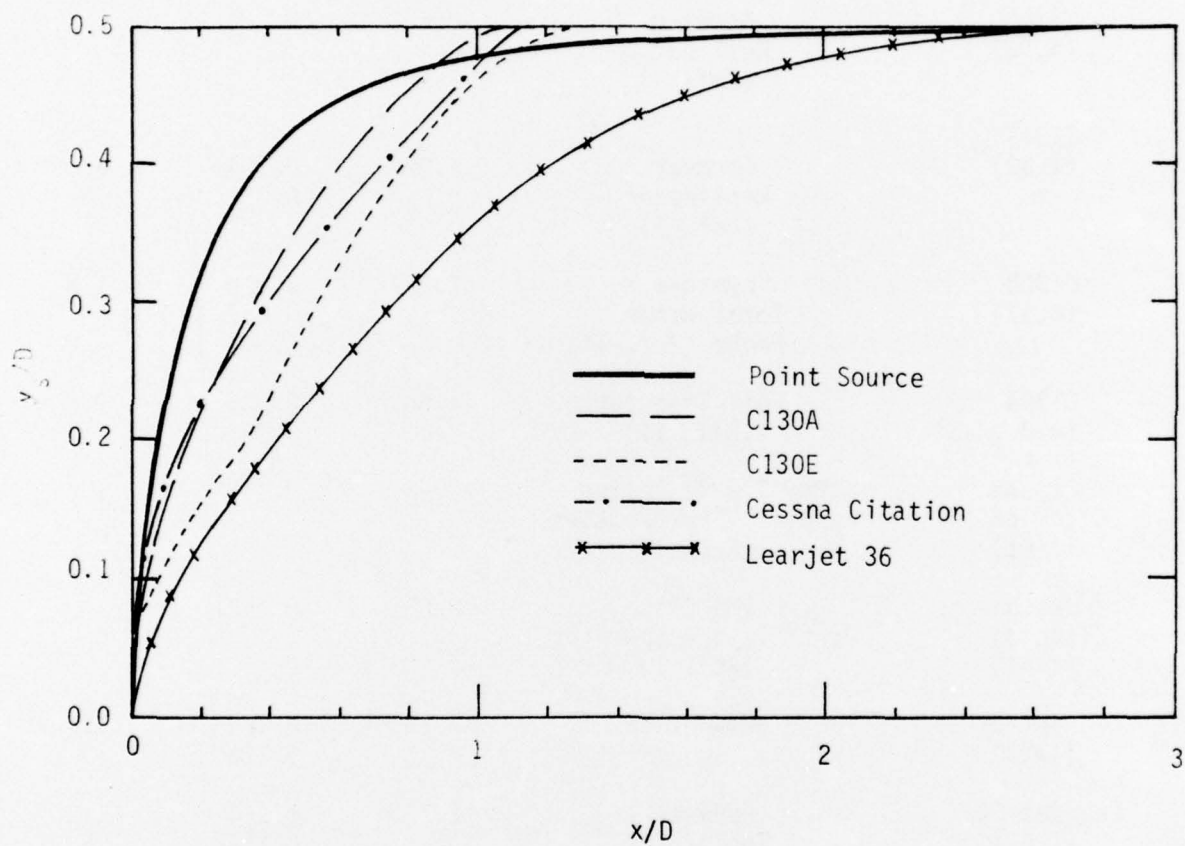


Figure 18. Fuselage radius, y_s vs. distance aft from the nose tip, x , for various airplane fuselages and the point source body. D is maximum fuselage diameter. See text for additional description.

Unfortunately there are not enough ice hydrometeor results available to warrant construction of similar graphs for ice. However, the reader should be aware that shadow zones are deeper, extend to larger particle masses and span broader ranges of sizes for ice as compared with water drops (see refs. 1 and 2).

SUMMARY AND CONCLUSIONS

Concentration factors for water drops were computed at the sampling points of three instruments mounted through the cabin windows of the Learjet 36 airplane: a PMS axial scattering probe, a snow stick and a formvar replicator. The largest concentration factor is 1.2 for 80 μm diameter drops at the snow stick, which instrument is the furthest aft of the three. To determine if the snow stick is shadowed for ice hydrometeors, concentration factors for ice columns and plates also were computed for that instrument; no shadowing was indicated. The distance of the shadow zone edge from the fuselage surface was determined approximately for each instrument.

Collection efficiency for hydrometeors of the Total Water Content Indicator (TWCI) mounted in the Learjet 36 nose was evaluated. To accomplish this, the concentration factor code was modified to allow intake of a specified fraction of the freestream flow by the TWCI orifice. Detailed examination of the air flowfield into and around the orifice showed that the computed flow is highly accurate. Hydrometeor flux tubes were calculated into the TWCI orifice for water drops and various ice crystal forms. Concentration factors substantially less than unity are found for small hydrometeors of all types except for ice crystal aggregates. Since freestream hydrometeor concentrations determined by the TWCI are proportional to reciprocal concentration factor (eq. (7)), large correction factors are required for most small hydrometeors (Fig. 12).

A preliminary version of a generalized graph by which "safe" water drop sampling distances for fuselage-mounted instruments can be estimated was prepared (Fig. 17). Potential airflow around an ideal point source was used as a convenient model of an airplane fuselage for the extensive concentration factor calculations required. Results for the point source body are compared with available case study results. Agreement is good for instruments mounted on the

cylindrical portions of fuselages. For instruments mounted on the forward (tapering) parts of fuselages, case study results indicate more shallow shadow zones than do the point source body results. This latter may be caused, at least in part, by the fact that the nose of the point source body affords the bluffest obstacle to flow of all shapes considered.

APPENDIX

VELOCITY FIELD EQUATIONS FOR POTENTIAL FLOW AROUND A SINGLE POINT SOURCE

The following is developed from chapter 16 of the book by Milne-Thompson⁽¹²⁾. The stream function, ψ , for unit freestream flow about a source of strength $1/4$ at the origin is

$$\psi = \frac{x}{4q} - \frac{r^2}{2} \quad (A.1)$$

where

$$q^2 = x^2 + y^2 + z^2$$

$$r^2 = y^2 + z^2$$

and freestream flow is parallel with the x axis and toward the positive x direction.

The velocity equations are

$$v_x = 1 + \frac{x}{4q^3} \quad (A.2)$$

$$\frac{v_y}{y} = \frac{v_z}{z} = \frac{1}{4q^3} \quad (A.3)$$

The body surface (defined by $\psi = -\frac{1}{4}$) is given by

$$r_s^2 = \frac{1}{2} \left(1 + \frac{x}{q_s} \right)$$

12. L.M. Milne-Thompson, Theoretical Hydrodynamics, fifth edition (The MacMillan Co., 1968).

which can be solved to give r_s as single valued function of x :

$$r_s = \sqrt{\frac{1}{2} (x \sqrt{x^2 + 2} + 1 - x^2)} \quad ; \quad x \geq -\frac{1}{2} . \quad (\text{A.4})$$

Equation (A.4) is used to calculate the surface contour of the body. The nose or stagnation point is at $x = -\frac{1}{2}$ and the body has unit radius ($r_s = 1$) at $x = \infty$.

REFERENCES

1. H.G. Norment and R.G. Zalosh, "Effects of Airplane Flowfields on Hydrometeor Concentration Measurements", AFCRL-TR-74-0602 (6 Dec. 1974). AD-A006 690.
2. H.G. Norment, "Effects of Airplane Flowfields on Cloud Water Content Measurements", AFCRL-TR-75-0231 (30 April 1975). AD-A014 807.
3. F.T. Krogh, "Variable Order Integrators for Numerical Solutions of Ordinary Differential Equations," Jet Propulsion Lab Technology Utilization Document No. CP-2308 (November 1970).
4. J.L. Hess and A.M.O. Smith, "Calculation of Non-Lifting Potential Flow About Arbitrary Three-Dimensional Bodies," McDonnell Douglas Report E.S. 40622 (15 March 1962). AD-282 255.
5. J.L. Hess and A.M.O. Smith, "Calculation of Potential Flow About Arbitrary Bodies," Progress in Aeronautical Sciences, Vol.8, edited by D. Kuchemann (Pergamon Press, New York, 1967).
6. C.N. Davies, "Definitive Equations for the Fluid Resistance of Spheres," Proc. Phys. Soc. (London) 57, 259-270 (1945).
7. S.R. Keim, "Fluid Resistance to Cylinders in Accelerated Motion," J. Hydraulics Div., Proc. Amer. Soc. Civil Eng., 6, paper 1113 (1956).
8. C.T. Crowe, J.A. Nicholls and R.B. Morrison, "Drag Coefficients of Inert and Burning Particles Accelerating in Gas Streams," Ninth Symp. (Int'l) on Combustion, Academic Press, pp. 395-405 (1963).
9. G.B. Foote and P.S. du Toit, "Terminal Velocity of Raindrops Aloft," J. Appl. Meteor. 8, 249-253 (1969).
10. R. Gunn and G.D. Kinser, "The Terminal Velocity of Fall for Water Droplets in Stagnant Air," J. Meteor. 6, 243-248 (1949).
11. H.G. Norment, "Effects of Airflow on Sampling of Water Drops by Two Instruments Mounted on the Fuselage of a Lockheed C130B Airplane," Final Report on Contract P.O. 01-6-022-11153 by Atmospheric Science Associates to Scientific Instrument Group, Research Facility Center, NOAA, Miami, Florida, Dec. 1, 1975.
12. L.M. Milne-Thompson, Theoretical Hydrodynamics, fifth edition (The MacMillan Co., 1968).